UDC 621
CODEN: MINSC5
ISSN 1857 – 5293
e-ISSN 1857 – 9191

MECHANICAL ENGINEERING SCIENTIFIC JOURNAL

МАШИНСКО ИНЖЕНЕРСТВО НАУЧНО СПИСАНИЕ

Volume 44
Number 1

Skopje, 2026

Mech. Eng. Sci. J.	Vol. **44**	No. 1	pp. 1–58	Skopje 2026
Маш. инж. науч. спис.	Год.	Број	стр.	Скопје

MECHANICAL ENGINEERING – SCIENTIFIC JOURNAL
МАШИНСКО ИНЖЕНЕРСТВО – НАУЧНО СПИСАНИЕ

Published by
Faculty of Mechanical Engineering, Ss. Cyril and Methodius University in Skopje, North Macedonia
Издава
Машински факултет, Универзитет „Св. Кирил и Методиј” во Скопје, Северна Македонија

Published twice yearly – Излегува два пати годишно

Editor in Chief	Одговорен уредник
Prof. Mite Tomov, Ph.D.	**Проф. д-р Мите Томов**
Co-editor in Chief	Заменик одговорен уредник
Prof. Taško Rizov, Ph.D.	**Проф. д-р Ташко Ризов**
Secretaries	Секретари
Doc. Marija Lazarevikj, Ph.D.	**Доц. д-р Марија Лазаревиќ**
Doc. Simona Domazetovska, Ph.D.	**Доц. д-р Симона Домазетовска**
Proof-reader	Коректор
Alena Georgievska	**Алена Георгиевска**
Technical editor	Технички уредник
Blagoja Bogatinoski	**Благоја Богатиноски**
UDC: Pandorka Stoimenovska	УДК: Пандорка Стоименовска
National and Universiti Library "St. Kliment Ohridski" – Skopje	НУБ „Св.. Климент Охридски“ – Скопје
Copies: 200	Тираж: 200
Price: 620 denars	Цена: 620 денари

Address
Faculty of Mechanical Engineering
(Mechanical Engineering – Scientific Journal)
Editor in Chief
P.O.Box 464
MK-1001 Skopje, Republic of North Macedonia

Адреса
Машински факултет
(Машинско инженерство – научно списание)
Одговорен уредник
пошт. фах 464
МК-1001 Скопје, Република Северна Македонија

Mech. Eng. Sci. J. is indexed/abstracted in INIS (International Nuclear Information System)
www.mf.ukim.edu.mk

MECHANICAL ENGINEERING – SCIENTIFIC JOURNAL
FACULTY OF MECHANICAL ENGINEERING, SKOPJE, REPUBLIC OF NORTH MACEDONIA

МАШИНСКО ИНЖЕНЕРСТВО – НАУЧНО СПИСАНИЕ
МАШИНСКИ ФАКУЛТЕТ, СКОПЈЕ, РЕПУБЛИКА СЕВЕРНА МАКЕДОНИЈА

Mech. Eng. Sci. J.	Vol.	No.	pp.	Skopje
	44	1	1–58	2026
Маш. инж. науч. спис.	Год.	Број	стр.	Скопје

TABLE OF CONTENTS
(С О Д Р Ж И Н А)

HYDRAULIC ENGINEERING
(Хидраулично инженерство)

ENERGY AND ENVIRONMENT
(Енергетика и животна средина)

MECHATRONICS
(Мехатроника)

Mechanical Engineering – Scientific Journal, Vol. **44,** No. 1, pp. 5–15 (2026)
Number of article: 700
Received: April 20, 2026
Accepted: May 12, 2026
In print: ISSN 1857–5293
On line: ISSN 1857–9191
UDC: [533.6:004.942]:621.548-42
https://doi.org/10.55302/MESJ2644105s

Original scientific paper

NUMERICAL INVESTIGATION OF AERODYNAMIC EFFICIENCY IN AN AIRFOIL TANDEM CONFIGURATION

Haritina Sakova[1*], Marija Lazarevikj[2], Zoran Markov[2]

[1]*Department of Aerospace Science and Technology, Politecnico di Milano, Italy*
[2]*Faculty of Mechanical Engineering, "Ss. Cyril and Methodius" University in Skopje, North Macedonia*
haritina.sakova@mail.polimi.it, //marija.lazarevikj@mf.edu.mk

A b s t r a c t: Tandem airfoils, used in the fields of aerodynamics for race cars and aircraft designs, are a key part of current research due to the aerodynamic complexity they introduce, while offering performance benefits. A numerical 2D CFD analysis of a tandem airfoil system was performed in this paper to determine their optimal positioning for achieving maximum aerodynamic efficiency and analyzing the resulting flow field. Simulations were conducted in Ansys Fluent using a high-quality mesh and refined boundary layer conditions, targeting $y^+ < 1$. Key parameters analyzed include the lift coefficient C_L, drag coefficient C_D, the C_L/C_D ratio, and flow visualizations such as pressure, velocity, streamlines, velocity vectors, and turbulent kinetic energy. Results indicate that the optimal angle of attack for the variable airfoil is −25°, where the highest C_L/C_D ratio is obtained. However, flow visualizations show wake formation at this angle, highlighting the need for further aerodynamic optimization to balance efficiency and wake reduction.

Key words: aerodynamic optimization; airfoils; CFD 2D analysis; numerical modeling

НУМЕРИЧКО МОДЕЛИРАЊЕ НА АЕРОДИНАМИЧНА ЕФИКАСНОСТ ЗА КОНФИГУРАЦИЈА НА ТАНДЕМ АЕРОДИНАМИЧНИ ПРОФИЛИ

А п с т р а к т: Тандемот на аеродинамичните профили, кои се користат во областа на аеродинамика за тркачки автомобили и за дизајн на авиони, е клучен дел од сегашни истражувања, поради аеродинамичната комплексност што ја создава. Во овој труд е извршена нумеричка анализа 2D CFD на систем од два аеродинамични профила, со цел да се дефинира нивната оптимална заемна поставеност за највисока аеродинамична ефикасност, а притоа да се опфати квалитетот на добиената струјна слика. Симулациите се спроведени со софтверскиот пакет Ansys Fluent, користејќи соодветна дискретизација и услови на граничен слој, со цел воспоставување вредност на $y^+ < 1$. Клучни параметри кои се предмет на анализата се коефициентот на подигање C_L, коефициентот на отпор C_D, односот C_L/C_D, струјната слика на притисокот, интензитетот на брзината, струјните линии, векторското поле на брзина, како и турбулентната кинетичка енергија. Резултатите покажуваат дека оптималниот агол на напад за променливиот аеродинамичен профил е −25°, при што се добива највисок C_L/C_D однос. Покрај тоа, струјните слики покажуваат формирање вртлози при оваа конфигурација, истакнувајќи ја потребата од понатамошна аеродинамична оптимизација, со цел балансирање на ефикасноста и намалување на отпорот кој е резултат на вртложното струење.

Клучни зборови: аеродинамична оптимизација; аеродинамични профили; анализа CFD 2D; нумеричко моделирање

1. INTRODUCTION

Computational Fluid Dynamics (CFD) has been developed as a scientific field by combining the laws of physics, numerical mathematics, and computer science in order to simulate flow phenomena that are difficult to obtain analytically [1, 2]. Its development has accelerated with the availability of powerful processors and advanced numerical methods, which enabled the solution of increasingly complex two-dimensional and three-dimensional flow problems [3, 4]. Later advances in viscous-flow simulation, based on the Navier–Stokes equations, led to the development of turbulence models

with different levels of complexity and accuracy [5]. Aerodynamics studies the forces and motion of bodies moving through air. In engineering analysis, CFD enables numerical simulation of airflow around aerodynamic bodies and provides a detailed representation of the resulting flow field. In this way, it becomes possible to interpret quantities such as velocity, pressure, wake development, and turbulence intensity around a profile or a multi-element configuration [6, 7].

Tandem airfoils are a configuration of two airfoils one behind the other along the flow direction, so the rear airfoil operates in the wake region of the front one [8]. They are used in many race car applications [9], as well as in modern aircraft designs [10]. Compared to a single airfoil, they have shown some efficiency improvements, while also introducing some trade-off decisions when designing this more complex aerodynamic system [11, 12, 13]. In addition to the pressure and velocity distributions generated around each element, the interaction between elements introduces wake effects, local flow separation, and increased turbulence [14]. These effects must be considered simultaneously when evaluating the overall aerodynamic response of the system. Previous numerical studies showed that the relative positioning of tandem airfoils significantly affects lift, drag, and wake interaction, making geometric optimization a key aspect of tandem-airfoil design. The present study is focused on a tandem airfoil configuration composed of NACA 6412 profiles. The usual angle of attack between them is below 30° [15]. One airfoil remains fixed, while the second is treated as a variable element whose angle of attack is changed in order to determine the most favorable relative arrangement. The analysis is based on two-dimensional RANS CFD simulations, as suggested by current literature [16] and includes evaluation of C_L, C_D, y^+, velocity field, pressure field, turbulent kinetic energy, streamlines, and velocity vectors. The goal is to identify the configuration that provides the most favorable aerodynamic response while also assessing the quality of the resulting flow field.

2. THEORETICAL BACKGROUND

2.1. *Governing equations*

The numerical analysis is based on the governing equations of fluid flow solved in ANSYS Fluent [17]. For viscous flow, the study is grounded in the Navier-Stokes formulation, while turbulence is modeled through the Reynolds averaged Navier-Stokes (RANS) approach. The RANS equation used as the basis of the turbulence model is:

$$\frac{\partial(\rho v_i)}{\partial t} + \frac{\partial(\rho v_i v_j)}{\partial x_j} = \\ = -\frac{\partial P}{\partial x_i} + \frac{\partial}{\partial x_j}\left[\mu\left(\frac{\partial v_i}{\partial x_j} + \frac{\partial v_j}{\partial x_i}\right) - \rho\overline{u_i' u_j'}\right] \quad (1)$$

where v_i is the mean flow velocity, u_i' are the velocity fluctuations, μ is the dynamic viscosity, and $-\rho\overline{u_i' u_j'}$ is the Reynolds stress tensor. Using the eddy-viscosity hypothesis, the Reynolds stresses are expressed as:

$$-\rho\overline{u_i' u_j'} = \mu_t\left(\frac{\partial v_i}{\partial x_j} + \frac{\partial v_j}{\partial x_i} - \frac{2}{3}\frac{\partial v_k}{\partial x_k}\delta_{ij}\right) - \frac{2}{3}\rho k\delta_{ij} \quad (2)$$

where μ_t is the turbulent viscosity, k is the turbulent kinetic energy, and δ_{ij} is the Kronecker delta.

2.2. *Realizable k- ε turbulence model*

For the present flow problem, the realizable k-ε model was selected because it is appropriate for simulations involving strong pressure gradients, possible flow separation, merging flow regions, asymmetry, and complex curved flow paths [18]. These characteristics are consistent with the expected flow around the tandem airfoil system.

The transport equation for turbulent kinetic energy is written as:

$$\frac{\partial(\rho k)}{\partial t} + \frac{\partial(\rho U_i k)}{\partial x_i} = \\ = \frac{\partial}{\partial x_j}\left[\left(\mu + \frac{\mu_t}{\sigma_k}\right)\frac{\partial k}{\partial x_j}\right] + P_k + P_b - \rho\varepsilon + S_k \quad (3)$$

The transport equation for the rate of turbulent dissipation is:

$$\frac{\partial(\rho\varepsilon)}{\partial t} + \frac{\partial(\rho U_i \varepsilon)}{\partial x_i} = \frac{\partial}{\partial x_j}\left[\left(\mu + \frac{\mu_t}{\sigma_\varepsilon}\right)\frac{\partial \varepsilon}{\partial x_j}\right] + \\ + \rho C_1 S_\varepsilon - C_2\rho\frac{\varepsilon^2}{k+\sqrt{\nu\varepsilon}} + C_1 C_3 \frac{\varepsilon}{k} P_b + S_\varepsilon \quad (4)$$

The turbulent viscosity is evaluated from:

$$\mu_t = C_\mu \rho \frac{k^2}{\varepsilon} \quad (5)$$

The model constants used are those generally accepted from Launder and Sharma [19].

2.3. *Aerodynamic coefficients and mesh-quality parameter*

For the two-dimensional configuration analyzed in this study, the aerodynamic response is expressed through non-dimensional section coefficients. The lift coefficient is given by [20]:

$$C_L = \frac{2F_L}{\rho v^2 l} \tag{6}$$

The drag coefficient is given by:

$$C_D = \frac{2F_D}{\rho v^2 l} \tag{7}$$

where F_L is the lift force, F_D is the drag force, ρ is the fluid density, v is the freestream velocity, and l is the airfoil chord length.

The near-wall mesh quality is evaluated by the dimensionless wall parameter y+, defined as [21]:

$$y^+ = \frac{\rho u_\tau y_P}{\mu} = \frac{u_\tau y_P}{\nu} \tag{8}$$

where u_τ is the friction velocity, y_P is the distance from the wall to the center of the first cell, μ is the dynamic viscosity, and ν is the kinematic viscosity.

The aerodynamic efficiency of the system is assessed through the ratio C_L/C_D but its interpretation must be supported by the corresponding flow-field visualizations, especially in cases where stronger loading is accompanied by larger wake formation and flow separation.

3. COMPUTATIONAL DOMAIN

There are several commonly used CFD packages considered for this type of analysis, namely ANSYS Fluent, COMSOL Multiphysics, and OpenFOAM. In this case ANSYS Fluent was selected as the most suitable solver for the present research because it offers a strong balance between precision, capability for complex simulations, and practical usability [22]. The analyzed configuration consists of two NACA 6412 airfoils arranged in tandem. The leading edges of the airfoils are separated by $A = 170$ mm in the streamwise direction and $B = 30$ mm in the transverse direction (Figure 1).

The chord length of each airfoil is $l = 200$ mm. The position of the elements is kept identical for all investigated cases, while the angle of attack of the second, variable airfoil is changed to $-15°$, $-20°$, and $-25°$ (Figure 1).

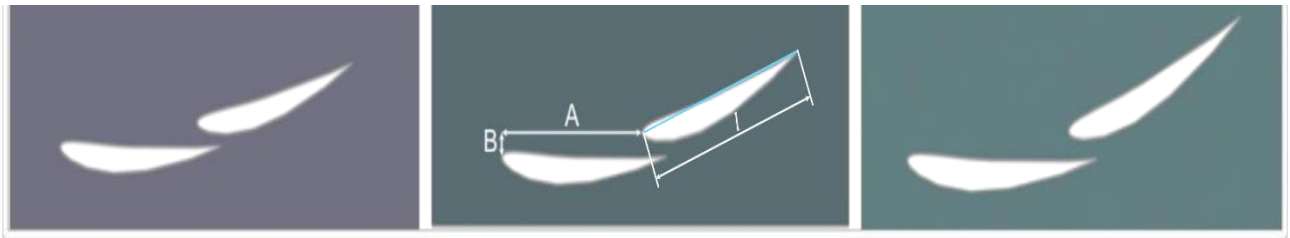

(a) (b) (c)

Fig. 1. Geometric definition of the tandem NACA 6412 configuration with A = 170 mm, B = 20 mm, and chord length l = 200 mm, under –15° (a), –20° (b), and –25° (c).

Since the configuration can be treated with a constant spanwise behavior, the analysis is carried out in a two-dimensional domain. The fluid domain was constructed in SolidWorks and sized according to the characteristic parameters proposed for double-element airfoil analysis [23]. The domain dimensions were defined so that: $C = 50 \cdot l$ and $D = 60 \cdot l$, as it can be seen on Figure 2. A rectangular subdomain of $3 \cdot 0.8\,m$ was additionally introduced around the airfoil system in order to enable local mesh refinement in the region of primary interest.

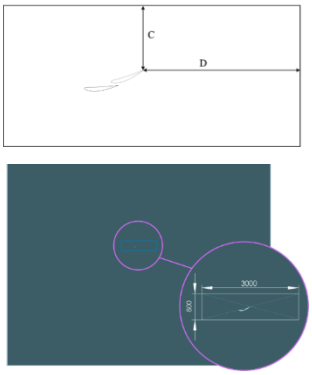

Fig. 2. Computational domain and local refinement region used for the tandem airfoil simulations.

3.1. *Mesh generation and near-wall treatment*

The computational domain was discretized using an unstructured triangular mesh. The mesh-generation procedure included: definition of the global maximum cell size, refinement of the rectangular zone around the profiles, edge division along the airfoil contours, introduction of inflation layers, and final mesh generation. Three mesh densities were initially tested in order to determine an appropriate balance between computational cost and accuracy. The dense mesh used a maximum element size of 0.1 m, the medium mesh 0.25 m, and the coarse mesh 0.6 m. The differences in the resulting values of C_L and C_D supported the selection of the medium mesh as an adequate compromise for the remaining simulations, as the differences were in the order of 10^{-3}, as it is depicted in Table 1.

T a b l e 1

Mesh selection analysis results

Type of mesh	Maximum elements size (m)	C_L	C_D
Fine	0.1	0.0925	–3.068
Medium	0.25	0.0928	–-3.069
Coarse	0.6	0,0928	–3.065

To ensure accurate near-wall resolution, the first boundary-layer cell height was set to $0.00002\ m$, the inflation region consisted of 15 layers, and the growth factor was 1.18. The mesh was designed so that the final simulations would retain $y^+ < 1$, which is suitable for resolving the near-wall region in the present study (Figure 3) [24].

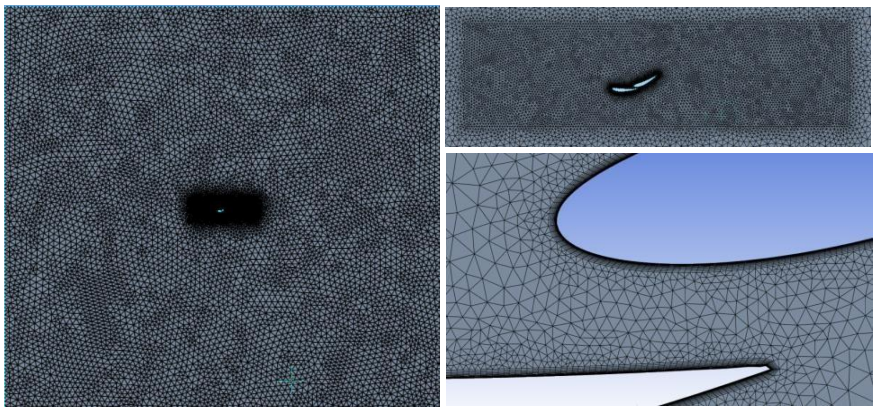

Fig. 3. Final discretization of the fluid domain

3.2. *Boundary conditions and simulation cases*

The boundary conditions were defined through inlet, outlet, fluid zone, wall boundaries, and the boundary layer around the airfoils. The outlet was prescribed through pressure-outlet conditions equal to atmospheric pressure.

The simulations were carried out at standard atmospheric pressure: $p_{atm} = 101325$ Pa and temperature: $T = 288.15$ K, for air with a density $\rho = 1.2250$ kg/m^3 and dynamic viscosity $\mu = 1.7894 \cdot 10^{-5}$ Pa·s. Only the flow field was of interest, therefore the energy equation was not included in the solution procedure.

The processing stage was carried out through 500 iterations for each of the nine cases. The residuals and monitored output parameters showed stabilization after approximately 150 iterations. Although literature may suggest lower continuity residuals as ideal, the residual level on the order of 10^{-4} obtained in this study was treated as acceptable for the intended engineering interpretation [25].

T a b l e 2

Operating cases of all performed simulations

Case number	v_{inlet} (m/s)	α (°)
1	11.11	
2	16.67	–15
3	22.22	
4	11.11	
5	16.67	–20
6	22.22	
7	11.11	
8	16.67	–25
9	22.22	

4. RESULTS AND DISCUSSION

4.1. *Numerical results*

The averaged numerical results obtained from ANSYS Fluent are summarized in Table 3. The table includes the lift coefficient, drag coefficient, wall parameter y^+, and the reported C_L/C_D ratio for all nine cases. The numerical data show that the absolute value of the lift coefficient increases as the angle of attack of the variable airfoil is increased from $-15°$ to $-25°$. At the same time, the drag coefficient also increases. This indicates that stronger aerodynamic loading is accompanied by stronger viscous phenomena. The largest magnitude of the lift coefficient is obtained at $v = 22.22\,m/s$ and $\alpha = -25°$, however, the **highest efficiency** is at the same velocity but at a lower angle of attack of $\alpha = \mathbf{-15°}$ (see highlighted data in Table 3). This shows the flow complexity and that higher lift does not correlate to overall higher efficiency.

An important outcome of the simulation is that all y^+ values remain below 1. The values vary between approximately 0.52 and 0.99, which confirms that the near-wall discretization was sufficiently refined for all simulated cases. As the velocity and the angle of attack increase, y^+ also tends to increase, which is consistent with the expectation of stronger gradients and more intense near-wall flow behavior.

Table 3

Numerical results for the tandem airfoil system

Velocity (m/s)	AOA (º)	Lift coefficient C_L	Drag coefficient C_D	y^+	C_L/C_D
11.11	–15	–3.0677023	0.092479007	0.52106687	–33.17187759
	–20	–3.6163794	0.11618891	0.53262596	–31.12499635
	–25	–3.8712711	0.15007215	0.5248618	–25.79606609
16.67	–15	–3.1142081	0.085772302	0.75516411	–36.30785262
	–20	–3.6736985	0.10732995	0.76528352	–34.22808359
	–25	–3.9461482	0.13926282	0.75589286	–28.33597797
22.22	–15	–3.1453805	0.081071928	0.9752026	–38.79740593
	–20	–3.7153239	0.10126909	0.99018781	–36.68763983
	–25	–4.0031303	0.13169004	0.97874969	–30.39812502

The original interpretation of the combined numerical and graphical results retained the $-25°$ configuration as the preferred arrangement. However, the numerical results alone are not sufficient for a final conclusion. For that reason, the flow field visualizations are essential for understanding whether the stronger aerodynamic loading is accompanied by undesirable wake growth and flow detachment.

4.2. *Velocity field*

The velocity contours provide the first direct insight into the aerodynamic behavior of the tandem configuration. For all investigated cases, shown in Figure 4, the velocity beneath the airfoils is higher than above them, which is consistent with the generation of a downforce. This is the key mechanism responsible for the downward aerodynamic loading of the system.

As the angle of attack of the variable airfoil increases, the flow behavior becomes progressively less attached near the trailing edge of that element. This effect is especially evident at the largest angle of attack, where a clear separation region appears behind the second airfoil. The tendency becomes even more pronounced as the freestream velocity increases.

The velocity contours therefore reveal two simultaneous tendencies. First, higher angle of attack increases the loading capability of the system. Second, the same increase promotes separation and wake formation. This means that the most aggressively loaded configuration also becomes the most vulnerable to aerodynamic losses generated by the disturbed downstream flow.

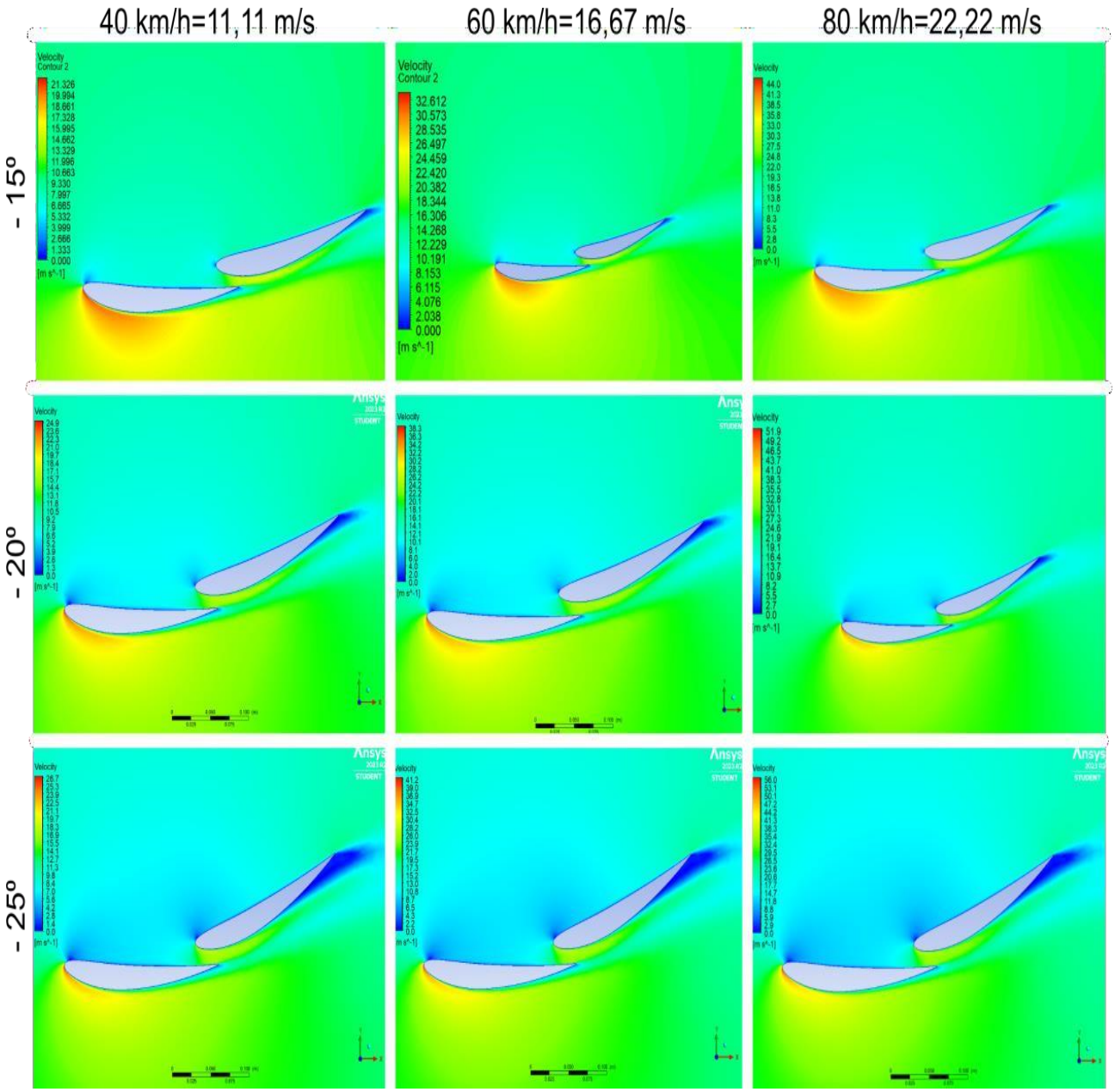

Fig. 4. Velocity contour distribution around the tandem airfoil system for the investigated inlet velocities and angles of attack

4.3. *Pressure distribution*

The pressure contours and pressure-distribution diagrams are consistent with the velocity field, as it can be observed in Figure 5. In accordance with Bernoulli-type interpretation of the flow, regions of higher local velocity coincide with reduced pressure, while the opposite occurs in regions of slower motion. Strong pressure differences are observed near the leading edges of both airfoils and along their surfaces.

The pressure field confirms that the airfoil pair produces substantial downward loading. At the same time, the pressure plots also indicate the onset of disturbed flow at the trailing edge of the variable airfoil. In the largest-angle cases, particularly at $-25°$, the pressure field shows stronger mixing between higher and lower pressure zones in the wake region. This is a clear sign of increasingly turbulent and separated flow.

Therefore, while the pressure gradients support stronger negative lift at higher angle of attack, they also highlight the aerodynamic cost of that choice. The pressure field does not simply confirm improved loading, but it also reveals the mechanism by which wake structures become stronger.

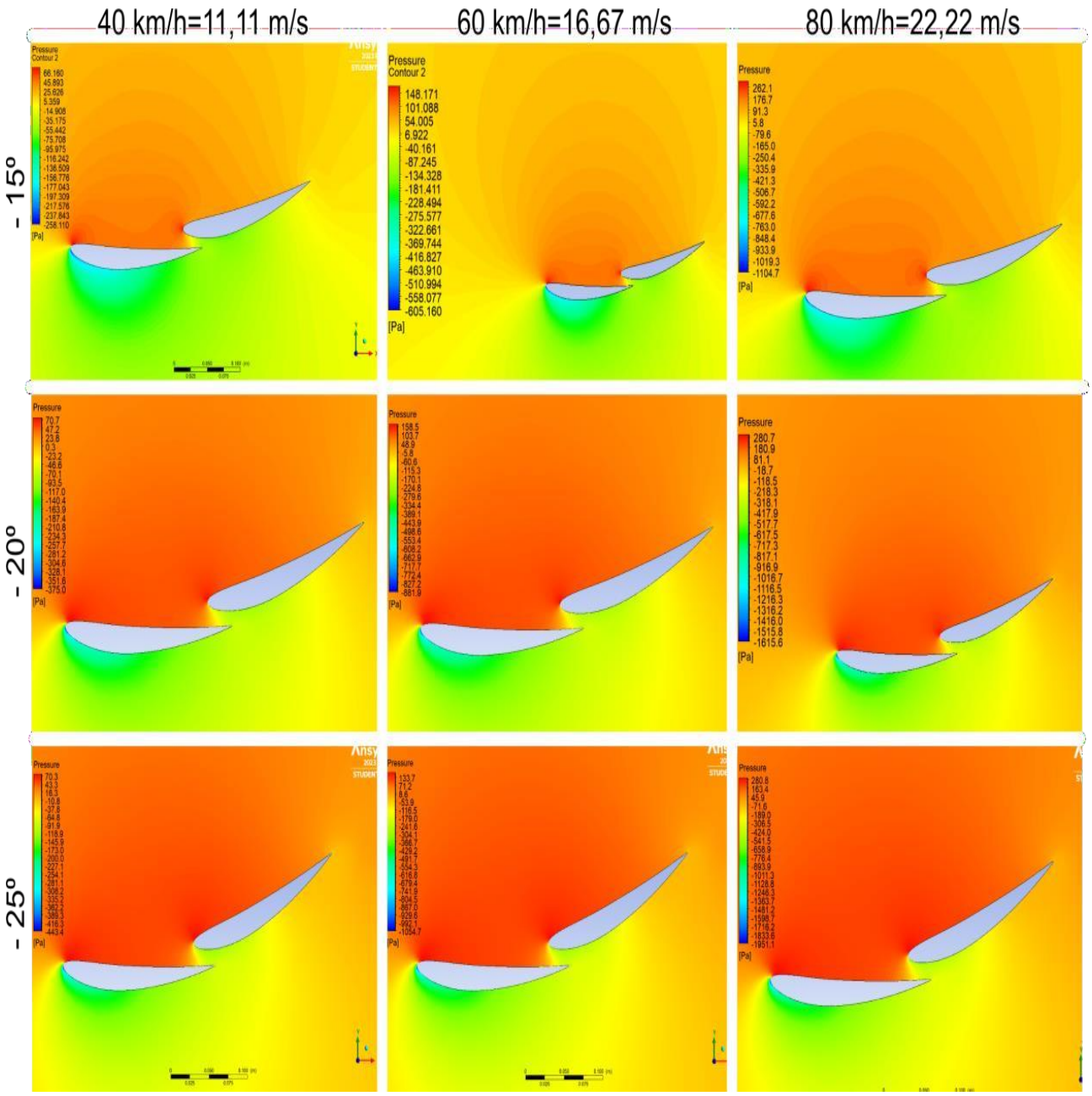

Fig. 5. Pressure contour distribution and surface-pressure behavior around the tandem airfoil system.

4.4. *Turbulent kinetic energy, streamlines, and velocity vectors*

The turbulent kinetic energy (TKE) contours in Figure 6 provide the clearest evidence of the wake intensity generated by the variable airfoil. The highest TKE values are concentrated behind the second airfoil, and the concentration becomes stronger as the angle of attack is increased.

In the wake region, the local velocity decreases strongly while the turbulent kinetic energy becomes large. This combination indicates the presence of intense turbulent structures immediately downstream of the variable element. The largest turbulence concentration is observed in the $-25°$ cases, where the trailing-edge separation is most visible.

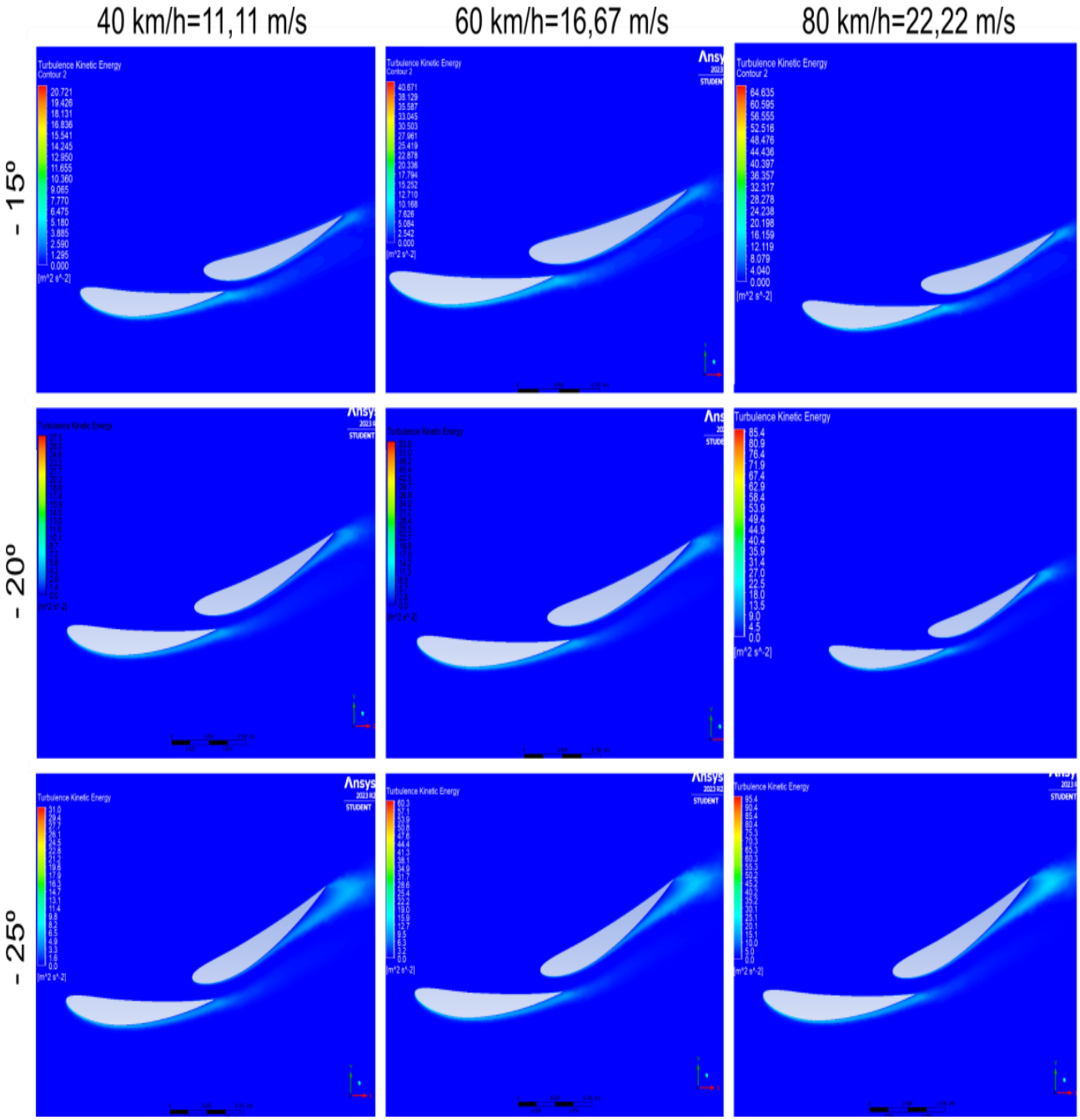

Fig. 6. Turbulent kinetic energy contours around the tandem airfoil system

In a streamline analysis shown in Figure 7, this was also visualized support the same conclusion. At higher angles of attack, the streamlines detach from the contour of the variable airfoil instead of following its surface smoothly. The velocity-vector plots additionally show the direction and local organization of the separated flow. The most pronounced vortex is observed for the case with $v = 22.22$ m/s and $\alpha = -25°$, where the wake structure behind the trailing edge is clearly developed.

Taken together, the graphical results show that the $-25°$ configuration is associated with the strongest aerodynamic loading but also with the largest wake, strongest turbulence, and clearest evidence of flow separation. This is the central trade-off of the present study. The preferred configuration reported by the original thesis is therefore not a fully optimized final solution, but rather the most promising configuration within the investigated range, provided that further refinement is introduced to reduce the downstream wake. A two-dimensional

CFD analysis of a tandem configuration composed of two NACA 6412 airfoils has been presented. The study investigated the effect of the angle of attack of a variable second airfoil at three inlet velocities and evaluated the aerodynamic response through numerical coefficients and flow-field visualizations.

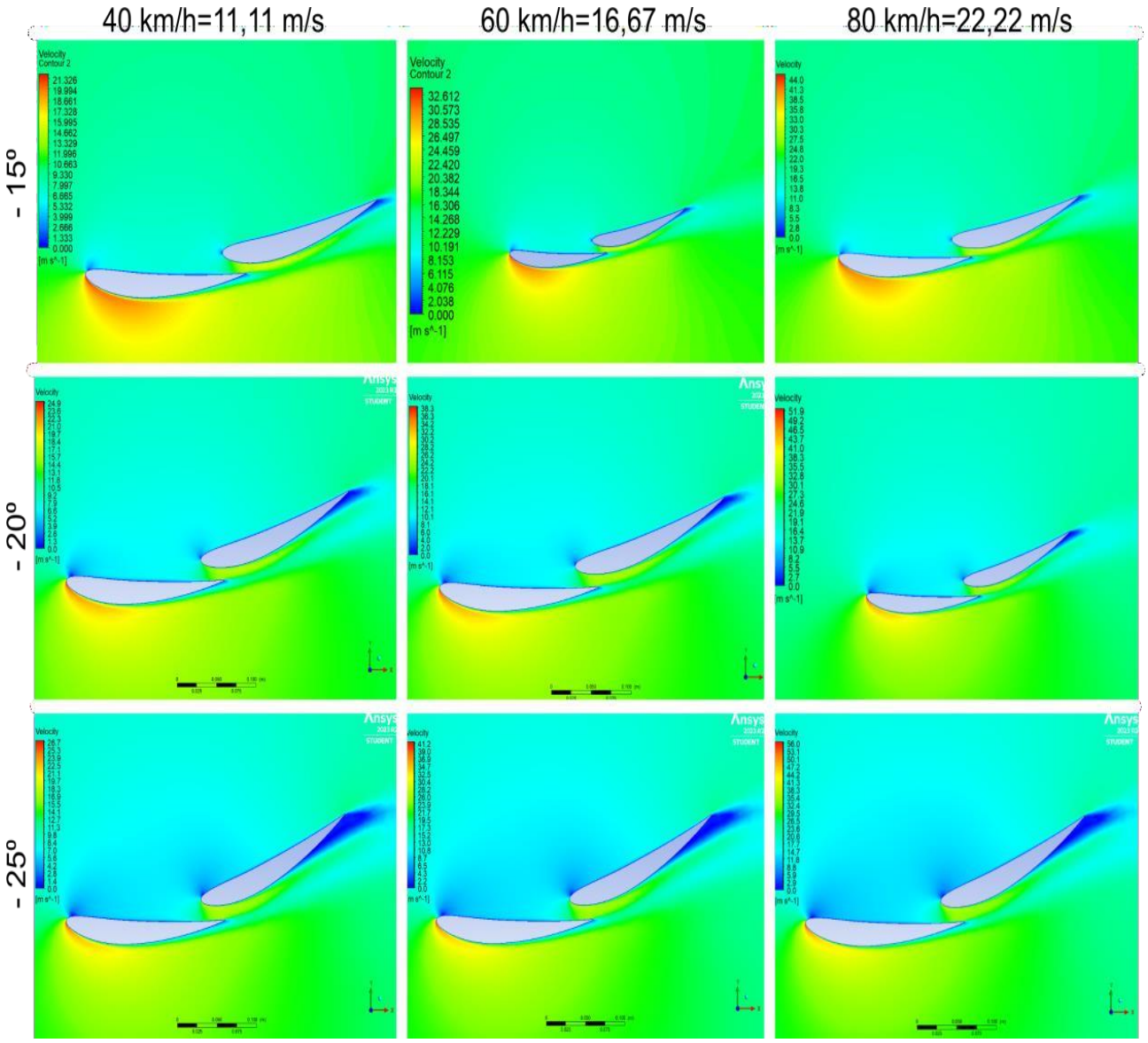

Fig. 7. Streamline contours based on velocity around the tandem airfoil system

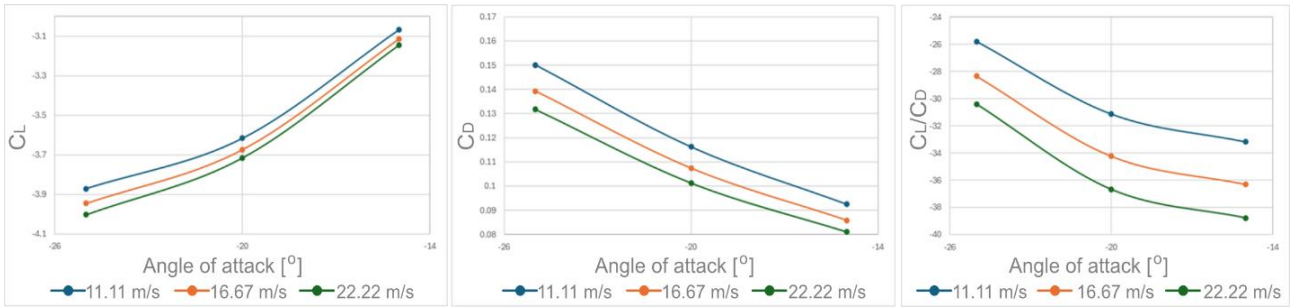

Fig. 8. Aerodynamic behavior within the tandem airfoil system, based on the a) lift coefficient, b) drag coefficient and c) efficiency ratio.

In Table 4 a representation of the change in lift drag and efficiency measure is reported. It can be noticed that with increase of the angle of attack, while the lift increases, the higher increase in drag lowered the overall efficiency for most cases. However, at higher velocities, hence at higher Reynolds numbers, this decrease of efficiency is less in all cases percentage-wise.

Table 4

Effects of changing the velocity and the angle of attack.

Velocity (m/s)	AoA (⁰)	Change in C_L (%)	Change in C_D %	Change in C_L/C_D %	Overall C_L/C_D change
11.11	–15				
	–20	17.9 ↑	25.6 ↑	6.2 ↓	
	–25	7.1 ↑	29. 2 ↑	17.1 ↓	28.6
16.67	–15				
	–20	17.97 ↑	25.1 ↑	5.7 ↓	
	–25	7.4 ↑	29.8 ↑	17.2 ↓	28.1
22.22	–15				
	–20	8.12 ↑	24.9 ↑	5.4 ↓	
	–25	7.75 ↑	30 ↑	17.1 ↓	27.6

5. CONCLUSION

The results show that increasing the angle of attack from -15° to -25° increases the magnitude of negative lift, but also increases drag and intensifies the wake behind the variable airfoil. The y^+ values remains below 1 in all nine cases, confirming satisfactory near-wall resolution and supporting the numerical reliability of the simulations.

The graphical analysis demonstrated that the most severe separation, largest turbulent kinetic energy, and strongest vortex structures occur in the -25° configuration, particularly at the highest investigated velocity. Nevertheless, based on the combined numerical and graphical interpretation presented in the original study, the -25° arrangement was retained as the preferred configuration among the three investigated angles. On another note, it was observed that at higher velocities, the increase in angle of attack is less significant when it comes to efficiency. Both the lift and drag coefficients increased, but due to the higher increase of drag, the overall efficiency always decreased.

The main conclusion is that the aerodynamic behavior of the tandem system is governed by a balance between stronger loading and stronger wake development. For that reason, the selected configuration should be understood as a promising basis for further optimization rather than a final solution. Future work should therefore be directed toward more advanced three-dimensional simulations and toward the introduction of additional aerodynamic elements capable of reducing separation and controlling the wake development without reaching stall conditions, as all performance would be compromised.

REFERENCES

[1] Blazek, J. (2001): *Computational Fluid Dynamics: Principles and Applications*, Alstom Power Ltd., Baden-Daettwil, Switzerland.

[2] Lazarevikj, M., Stojkovski, F., Iliev, I., Markov, Z. (May 2019): Influence of the guide vanes design on stress parameters of Francis 99 turbine, Third Francis 99 Workshop, NTNU, Trondheim, Norway, *Journal of Physics: Conference Series*, Volume 1296, 012008, https://doi.org/10.1088/1742-6596/1296/1/012008

[3] Rumsey, C. L., Ying, S. X. (2002): Prediction of high lift: review of present CFD capability, *Journal of Progress in Aerospace Sciences*, vol. **38**, no. 2, pp. 145–180, https://doi.org/10.1016/S0376-0421(02)00003-9,

[4] Lazarevikj, M., Stojkovski, F., Markov, Z., Iliev, I., Dahlhaug, O. G. (2022): Parameter based tool for Francis turbine guide vanes design using coupled MATLAB –

ANSYS approach, *J. Sustain. Dev. Energy Water Environ. Syst*., Vol. **10**, Iss. 3, 1090410, DOI: https://doi.org/10.13044/j.sdewes.d9.0410

[5] Crochet M. J. (1989): Numerical simulation of viscoelastic flow: a review, *Rubber Chemistry and Technology*, vol. **62**, no. 3, pp. 426–455. DOI:10.5254/1.3536253

[6] N.N.: What is CFD | Computational Fluid Dynamics?, SIMSCALE, https://www.simscale.com/docs/simwiki/cfd-computational-fluid-dynamics/what-is-cfd-computational-fluid-dynamics/

[7] Hall, N.: Guide to Aerodynamics, NASA, https://www1.grc.nasa.gov/beginners-guide-to-aeronautics/learn-about-aerodynamics/

[8] Fanjoy, D. and Dorney, D. (May 1, 1996): Numerical simulations of tandem-airfoil aerodynamics, *Aerospace Atlantic Conference & Exposition*, Dayton, Ohio, United States. https://doi.org/10.4271/961295.

[9] Delikan, M., Bal, Ş. (2025): A comprehensive CFD analysis of tandem foils with and without ground effect. *J Nav Archit Mar Technol*. **227** (1), pp. 1–21. DOI: 10.54926/jnamt.2025.247.

[10] Kryvokhatko, I. (2025): *Aerodynamics of Tandem Wing Aircraft*, 2nd edition,

[11] Fangzheng, C., Jianqiao, Y., Yuesong, M. (2017): Aerodynamic design optimization for low Reynolds tandem airfoil", Proceedings of the Institution of Mechanical Engineers, Part G. *Journal of Aerospace Engineering*, **232** (6): 095441001770421,

[12] Rajosik Adak et al. (2022): Aerodynamic performance of a tandem wing configuration inspired from dragonfly gliding flight for MAV application, Department of Aerospace Engineering, IIT Kharagpur.

[13] Anderson K. W. et al.: Navier-Stokes Computations and Experimental Comparisons for Multielement Airfoil Configurations, NASA Langley Research Center, Hampton, VA 23681, url: https://fun3d.larc.nasa.gov/papers/ja93.pdf

[14] Faure T. M. et al. (2017): Aerodynamic features of a two-airfoil arrangement, *Experiments in Fluids*. **58**, 146 https://doi.org/10.1007/s00348-017-2429-4

[15] Bikić, S., Todorović, B., Bukurov, M., Radojčin, M., Pavkov, I. (2018): Accuracy analysis of air torque position dampers based on blade profiles and damper locations, *Therm. Sci*. **22** (1B), 675–685. https://doi.org/10.2298/TSCI160805174B

[16] Chaiyanupong, J., Khajorntraidet, C. (2024): Design and analysis of double element airfoil using RANS, *Journal of Research and Applications in Mechanical Engineering*, vol. **12**, no. 1. Paper No. JRAME-24-12-003.

[17] N. N.: Ansys Fluent - Fluid Simulation Software, ANSYS, https://www.ansys.com/products/fluids/ansys-fluent

[18] N. N.: K-Epsilon Turbulence Models, SIMSCALE. https://www.simscale.com/docs/simulation-setup/global-settings/k-epsilon/

[19] Launder, E., Sharma, B. I. (1974): Application of the energy dissipation model of turbulence to the calculation of flow near a spinning disc, *Letters in Heat and Mass Transfer*, vol. **1**, pp. 131–138.

[20] N. N.: What is Lift Coefficient?, SIMSCALE. https://www.simscale.com/docs/simwiki/lift-drag-pitch/what-is-lift-coefficient/

[21] N. N.: Y-Plus Application in CFD Simulation, MR CFD. https://www.mr-cfd.com/y-plus-application-in-cfd-simulation/

[22] N. N.: Top Computational Fluid Dynamics (CFD) Software, Technology Evaluation Centers. https://www3.technologyevaluation.com/c/computational-fluid-dynamics-cfd

[23] Anderson, J.: Fluids – Lecture 19: Airfoils – Overview, MIT. https://web.mit.edu/16.unified/www/FALL/fluids/Lectures/f19.pdf

[24] N. N.: Calculators and Tools, FluidMechanics101. https://www.fluidmechanics101.com/pages/tools.html

[25] Stern, F., Wilson, R. V., Coleman, H. W., Paterson, E. G. (1999): *Verification and Validation of CFD Simulations*, Iowa Institute of Hydraulic Research & Propulsion Research Center, Mechanical and Aerospace Engineering Department, University of Alabama in Huntsville.

Mechanical Engineering – Scientific Journal, Vol. **44,** No. 1, pp. 17–25 (2026)
Number of article: 701 ISSN 1857–5293
Received: May 12, 2026 e-ISSN 1857–9191
Accepted: June 10, 2026 UDC: [502.3:613.15]:33.024(497.711)"2016/2025"
https://doi.org/10.55302/MESJ2644117s

Original scientific paper

ASSESSMENT OF AIR QUALITY MANAGEMENT STRATEGIES IN SKOPJE: LONG-TERM PM TRENDS AND REGULATORY COMPLIANCE 2016–2025

Andrej Stojkovski, Marija Lazarevikj, Monika Uler-Zefikj, Zoran Markov, Dame Dimitrovski

Faculty of Mechanical Engineering, "Ss. Cyril and Methodius" University in Skopje,
P.O. Box 464, MK-1001 Skopje, Republic of North Macedonia
a.stojkovski2942@student.mf.ukim.edu.mk

A b s t r a c t: Air quality remains a persistent challenge in urban environments, particularly in cities with complex emission structures and seasonal variability. This paper investigates air quality management strategies in Skopje from 2016 to 2025, emphasizing particulate matter (PM) concentrations and long-term pollution trends. The methodology integrates multi-year monitoring data with statistical processing, graphical interpretation, and an assessment of dominant emission sources. A significant portion of the study evaluates the relationship between national regulatory practices and the European Union framework to determine practical alignment. By synthesizing technical observations with the regulatory context, this paper offers a grounded perspective on the evolution of air quality management over the analyzed decade.

Key words: air quality; particulate matte;, urban pollution; regulatory alignment

ПРОЦЕНА НА СТРАТЕГИИТЕ ЗА УПРАВУВАЊЕ СО КВАЛИТЕТОТ НА ВОЗДУХОТ ВО СКОПЈЕ: ДОЛГОРОЧНИ ТРЕНДОВИ НА PM ЧЕСТИЧКИТЕ И УСОГЛАСЕНОСТ СО РЕГУЛАТИВАТА 2016–2025

А п с т р а к т: Квалитетот на воздухот претставува постојан предизвик во урбаните средини, особено во градовите со комплексни емисиони структури и сезонска варијабилност. Овој труд ги истражува стратегиите за управување со квалитетот на воздухот во Скопје во периодот 2016–2025 година, со акцент на концентрациите на суспендираните честички (PM) и долгорочните трендови на загадување. Методологијата интегрира повеќегодишни податоци од мониторинг со статистичка обработка, графичка интерпретација и процена на доминантните извори на емисија.Значителен дел од студијата го оценува односот помеѓу националните регулаторни практики и рамката на Европската Унија за да се утврди практичната усогласеност. Преку синтеза на техничките набљудувања со регулаторниот контекст, трудот нуди перспектива за еволуцијата на управувањето со квалитетот на воздухот втемелена во анализираниот период.

Клучни зборови: квалитет на воздух; суспендирани честички; урбано загадување; регулаторна усогласеност

INTRODUCTION

Ambient air pollution is a major environmental and public health concern [1]. Across European urban centers, it remains one of the most critical challenges, driving urgent regulatory reforms [2]. Specifically, Skopje has historically experienced severe exceedances of particulate matter limit values, generating substantial socio-economic and health implications [3]. Alongside anthropogenic emissions from heating and traffic, the city's specific urban morphology and continuous spatial expansion further complicate the effective dispersion of pollutants [4]. The primary objective of this work is to systematically evaluate the evolution of air quality management strategies over a decade. Driven by the complex interaction of these emission

sources and meteorological conditions, Skopje serves as a representative urban case study.

The city's valley topography severely limits horizontal airflow. During winter, frequent temperature inversions reduce vertical exchange, causing the Planetary Boundary Layer (PBL) altitude to frequently drop below 200 m [5]. This fundamentally dictates the volume available for pollutant dispersion and drastically increases PM concentrations. Furthermore, radiational cooling at night forms a highly stable, shallow nocturnal boundary layer that traps ground-level emissions. Morning solar radiation then increases the PBL height, improving vertical mixing. These diurnal PBL oscillations are a key mechanism driving the daily variability of pollution.

To address these severe physical limitations on pollutant dispersion, robust regulatory frameworks are essential. While the national "Ambient Air Quality Act" [6] mandates institutional air quality planning, it lacks specific legal instruments for individual protection. In contrast, the new EU Directive 2024/2881 [7] introduces legal liability and the right to compensation for health damages caused by non-compliance with air quality standards (Article 28), transforming regulation from mere governance into strict accountability.

While existing studies extensively document the localized health impacts and meteorological drivers of pollution in Skopje, there is a notable gap in synthesizing long-term technical monitoring data with the evolving legal frameworks. Previous literature lacks a comprehensive, decade-long analysis of pollution trends across different urban zones, evaluated directly against the stringent new European standards. To address this, the present study provides a combined long-term statistical and regulatory assessment of air quality in the city in the period of 2016–2025. The scientific added value of this research lies in integrating advanced heatmap visualizations of a ten-year continuous dataset with a direct comparative analysis between national legislation and the newly introduced EU Directive 2024/2881, offering a practical perspective on urban air quality management.

METHODOLOGY

The research methodology is structured into four distinct phases: data collection, data preprocessing, data processing, and data visualization and analysis, as illustrated in the flowchart in Figure 1.

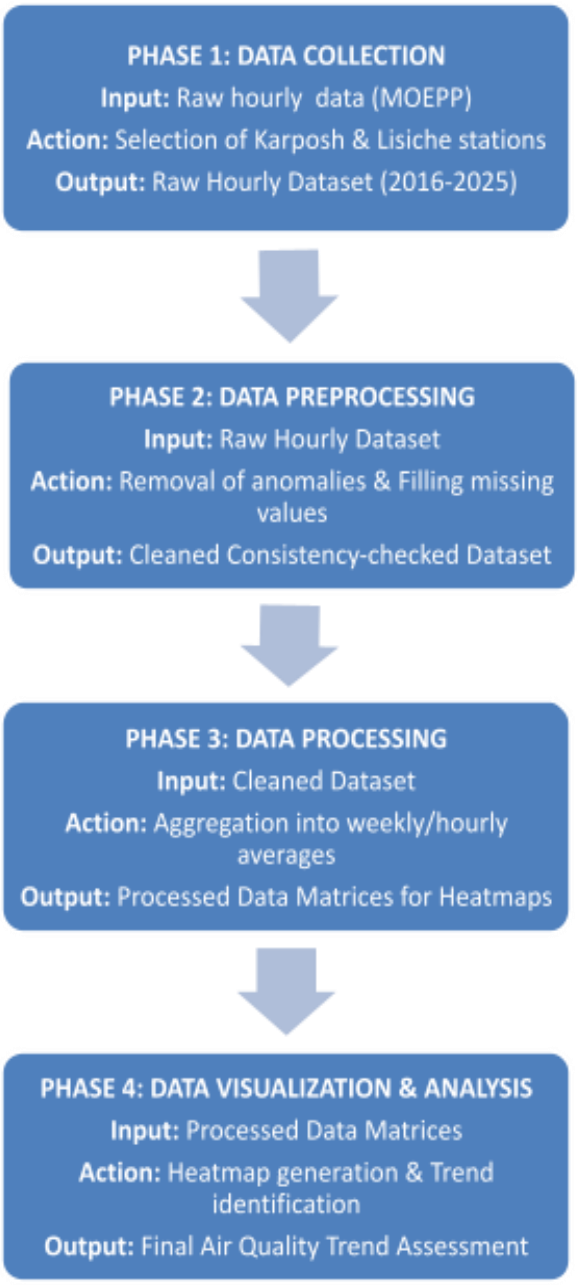

Fig. 1 Flowchart of the four-phase air quality assessment methodology

Phase 1: Data collection: The initial phase involved the acquisition of raw hourly data for particulate matter ($PM_{2.5}$ and PM_{10}) from the authorized State Automatic Air Quality Monitoring System (SAAQMS), governed by the Ministry of Environment and Physical Planning (MOEPP). The analyzed dataset spans a comprehensive 10-year period, from January 2016 to December 2025. To capture the spatial distribution of pollutants and the diverse urban microenvironments within the Skopje agglomeration, two specific monitoring stations

were selected: Karposh and Lisiche. This selection was not random but based on their distinct geographical positioning (Karposh in the western part, and Lisiche in the eastern part of the city) and their varying proximity to major emission sources. Together, these locations provide a representative overview of the three primary types of polluters: industrial facilities, urban traffic, and residential households. The exact geographical coordinates of the stations were provided by MOEPP. Furthermore, all measurements were recorded at a standard height of 1.5 meters above ground level, which accurately represents the average human inhalation height for ambient air.

Phase 2: Data preprocessing: Following data retrieval, the raw hourly datasets were integrated into Microsoft Excel for preprocessing. This phase included systematic data sampling and the rigorous removal of measurement anomalies. Specifically, negative values resulting from instrument calibration errors and extreme outliers exceeding three standard deviations (the 3-sigma rule) from the weekly mean were excluded. To ensure temporal continuity without distorting the statistical baseline, isolated data gaps of one to two hours were addressed using linear interpolation. Larger missing intervals were reconstructed utilizing mean diurnal profile imputation for the respective month, thereby preserving the natural seasonal variance of the dataset prior to further analysis.

Phase 3: Data processing: The cleaned dataset was subsequently processed to extract meaningful temporal trends. Using time-series aggregation and arithmetic averaging in Excel, the data matrices were structured. This involved the precise calculation and adoption of values to generate average weekly profiles and average hourly profiles, allowing for the isolation of specific pollution peaks related to time of day or day of the week.

Phase 4: Data visualization and analysis: In the final phase, the processed data matrices were utilized to construct heatmaps for trend identification. The heatmaps were developed entirely within Microsoft Excel using custom formulas and conditional logic. A continuous color gradient was applied to visually represent pollution intensity: green indicates minimal pollution values (clean air), progressively transitioning through darker shades as concentrations increase, culminating in dark red, which signifies the maximum recorded pollution values (heavily polluted ambient air). This visualization method directly correlates temporal patterns with the exact intensity of the aerosol pollution.

RESULTS AND DISCUSSION

Temporal distribution and heatmap analysis

The long-term temporal dynamics of PM_{10} concentrations in Skopje are visualized through heatmap diagrams for the Karposh (Table 1) and Lisiche (Table 2) monitoring stations. These diagrams map average weekly values over a ten-year period. The numerical values presented within these specific heatmaps represent the average weekly concentrations of PM_{10}. These weekly arithmetic means were derived by aggregating the preprocessed base dataset of continuous hourly measurements over the ten-year period (2016–2025). This level of temporal aggregation was selected to smooth out short-term daily anomalies while effectively highlighting broader intra-annual pollution patterns.

The analysis indicates a clearly expressed seasonal variability, with high-concentration zones consistently localized in the winter months (weeks 1–8 and 46–52). This specific winter period corresponds to the peak heating season and is characterized by stable atmospheric conditions and a reduced Planetary Boundary Layer (PBL) height.

- Karposh station analysis: The patterns in Karposh show a more uniform distribution during transitional periods, likely due to the continuous influence of traffic emissions. However, even here, a noticeable cooling of colors (reduction in intensity) is observed in the middle section of the heatmap (weeks 15–35) across the years.
- Lisiche station analysis: The Lisiche heatmap shows significantly higher intensities compared to Karposh, particularly during the winter months. The "winter blocks" in Lisiche are more persistent, confirming the heavy impact of domestic heating with solid fuels in this residential area.
- Station comparison and trends: A comparison of the two locations reveals that Lisiche consistently exhibits 20–30% higher peak concentrations than Karposh during winter episodes. Quantitatively, the analysis between 2016 and 2025 indicates a significant improvement. In Karposh, annual average PM_{10} levels decreased by 48.3% (from 60.1 to 31.1 μg/m³), while Lisiche showed a 36.7% reduction (from 79.1 to 50.1 μg/m³). While summer concentrations remain relatively constant, the most significant reductions are observed during the transitional and winter heating periods.

Table 1

Heatmap diagram of PM_{10} concentrations at the Karposh monitoring station (2016–2025), illustrating seasonal variability and recurring high-concentration periods

Karposh PM10 (weekly)	Average weekly value expres sed in μg/m^3									
	2016	2017	2018	2019	2020	2021	2022	2023	2024	2025
1	182.56120	91.44872	123.31770	56.62316	95.97423	43.57508	79.47143	112.71770	103.61530	75.82043
2	74.31954	202.67620	99.48969	88.50186	93.37574	32.25149	53.18730	54.66958	54.51989	49.17936
3	75.52323	149.36090	61.08989	184.2088	58.63337	113.67340	46.77842	47.56213	65.60342	45.28156
4	171.37460	177.80170	111.65490	71.64726	122.80550	40.47786	61.92285	20.24847	40.10242	75.52399
5	80.12107	268.34070	115.56090	115.5683	95.29230	74.77736	71.57192	37.46883	66.24348	52.81936
6	61.78221	73.74274	67.63859	54.84367	48.10064	43.14440	52.18345	51.89683	102.71700	47.51001
7	56.44329	101.12320	60.49661	38.4974	67.35926	85.69476	63.25355	67.04438	45.09261	55.67441
8	56.57347	87.56284	37.11607	75.83544	55.70456	73.52352	35.77959	50.87795	46.37467	42.73810
9	37.22364	66.19157	62.81000	49.56776	48.38952	50.21358	49.85753	38.92049	39.85993	47.33244
10	35.53433	35.89087	48.96774	66.58307	32.39596	53.52090	33.81413	37.60614	26.82423	43.10547
11	34.78659	48.49297	45.19760	46.6313	35.17288	28.89199	47.98573	29.72197	26.00280	39.48523
12	38.57724	58.52119	38.57076	38.96651	40.84826	38.62813	39.36827	39.20333	28.99315	27.03661
13	50.79199	38.75446	39.61183	42.87281	44.37941	31.33099	42.80673	22.37894	29.25106	19.99217
14	44.20056	28.10580	34.41134	47.68231	33.11706	27.81780	28.55027	22.86277	33.57013	13.09713
15	40.07163	34.01651	53.61620	20.85083	27.12182	26.93147	30.53695	20.46636	36.21519	22.17650
16	37.50890	21.20526	39.60990	26.85436	28.24887	25.33556	26.95451	21.30057	23.60881	17.61566
17	21.78841	40.52203	46.22379	49.43697	24.22082	38.97549	22.42846	23.71989	15.37174	16.16186
18	18.74104	38.64804	44.35433	24.86283	22.16746	27.05174	25.02911	20.52822	15.46366	20.01056
19	26.65869	28.69169	29.06564	25.19376	21.90993	22.49387	32.84791	17.31142	14.72059	18.85910
20	22.36131	26.31447	22.29460	24.18371	45.94420	24.36598	26.49547	26.60126	19.81221	13.25547
21	27.23349	23.41117	27.05357	22.16750	31.65895	31.77810	39.49049	22.80884	21.65453	15.45376
22	26.97460	27.55042	34.18114	–	15.52020	26.22417	34.52614	22.40078	23.57344	14.75524
23	24.25271	28.37833	29.72357	–	21.63581	29.30227	27.33287	26.38415	29.89156	24.23007
24	24.60370	30.63860	31.40862	46.00077	23.49700	28.18472	24.48960	18.55170	37.85811	22.03135
25	42.88807	34.99176	25.45899	33.50267	15.44317	52.71544	36.53592	31.76894	52.13440	19.81240
26	30.22557	48.26363	21.84719	–	20.48651	40.25627	31.45673	21.22618	28.23030	22.37524
27	24.48416	31.18580	33.97461	32.17873	27.95412	36.83772	29.17820	23.11870	22.83049	19.73321
28	30.89600	33.73711	27.63574	30.38013	27.36991	34.97265	–	34.00774	34.00709	19.75684
29	28.20360	36.09125	30.93781	–	22.83910	28.06892	31.26793	37.25939	34.89667	18.71853
30	35.33226	31.11299	24.57169	27.67323	19.01017	47.47722	29.19150	20.51528	22.99174	34.79323
31	32.57830	38.62851	31.06987	26.59503	22.15887	47.14270	25.24438	24.82698	27.95010	13.93669
32	26.92590	44.65187	35.95551	–	24.74570	33.02322	20.52926	18.37960	19.85799	17.09317
33	44.48154	35.87954	32.03443	27.78287	–	28.43257	29.14734	33.31627	37.57757	26.80184
34	28.66051	31.80164	34.27459	42.70190	–	37.62453	31.72647	38.69202	24.52940	18.24733
35	42.73030	39.19270	32.72446	39.86597	–	25.46464	25.19068	25.22642	34.28607	24.48689
36	42.52754	32.77221	31.75764	39.51707	–	28.74853	21.30820	27.59800	51.79239	18.66869
37	61.83666	36.94603	34.30400	33.96176	–	40.39662	22.82322	35.34971	13.25363	23.36657
38	37.26067	29.59374	46.23320	32.36835	–	26.65276	15.78434	44.05665	15.42695	19.33077
39	67.13931	28.94846	34.43549	30.92547	–	33.97154	25.09577	31.65312	24.00619	21.12807
40	47.79514	37.86460	46.57454	29.52047	31.06047	25.98606	28.05421	34.31919	17.96864	10.30657
41	66.91759	53.97864	43.58766	38.00127	32.52072	14.26250	31.94263	50.79380	17.18819	12.51896
42	33.84209	87.94297	62.34853	55.13636	21.99789	48.19015	36.26293	35.28338	26.03383	22.66496
43	68.92306	34.75450	49.05707	74.64382	55.27790	66.10764	37.76416	37.91788	43.99203	26.36680
44	82.11958	70.37434	73.30069	44.76658	47.07670	56.03758	55.58927	28.99420	39.55801	28.29567
45	54.15353	89.05047	101.72560	33.86322	64.48902	52.46002	46.47875	28.80036	60.07709	24.55001
46	122.08500	44.52933	85.56866	48.34937	114.6545	69.98255	56.55923	30.66173	29.79906	36.74447
47	141.0769	120.08740	60.19500	46.43100	68.51273	54.24000	28.76502	29.86216	40.30739	24.04859
48	83.16847	56.22856	70.28774	42.88383	141.56340	56.13800	59.25830	45.44793	47.60940	22.35417
49	216.3018	97.88880	138.19740	81.63167	96.85448	37.63568	47.72418	59.60908	29.35347	42.42966
50	121.8411	185.63180	74.48090	56.17770	61.04939	26.22426	34.08209	43.14992	39.84603	53.46763
51	221.87980	40.81356	102.15040	52.59775	47.27292	112.46102	114.01230	93.16704	52.61041	145.29510
52	46.05465	107.51610	92.19563	16.73401	84.03221	66.00155	123.14260	157.12230	24.26330	42.70976
Annually	60.13769	63.42649	53.60008	48.89023	48.96683	41.75828	39.17898	37.21285	34.97302	31.07103

Table 2

Heatmap diagram of PM_{10} concentrations at the Lisiche monitoring station (2016–2025), illustrating seasonal variability and recurring high–concentration periods

Lisiche **PM10 (weekly)**	Average weekly value expressed in µg/m³									
	2016	2017	2018	2019	2020	2021	2022	2023	2024	2025
1	258.7	138.8	207.5	–	171.1	44.4	109.7	147.9	130.9	150.2
2	102.9	225.9	144.7	–	133.5	40.9	67.5	73.6	66.7	116.2
3	110.0	162.4	83.8	–	79.4	130.2	75.0	70.2	116.8	72.1
4	252.9	207.5	151.8	–	183.8	61.9	71.8	29.7	35.5	100.3
5	128.6	331.5	150.0	–	158.2	147.1	94.6	56.7	109.7	102.5
6	91.6	109.7	92.8	–	70.0	53.4	66.0	89.4	138.8	73.9
7	68.2	116.5	92.1	–	107.0	131.3	79.0	127.0	69.9	76.4
8	68.7	110.8	44.1	–	74.4	130.2	43.4	91.7	60.2	58.6
9	41.4	69.0	80.7	–	63.4	79.9	51.3	42.1	46.6	65.5
10	37.7	35.3	58.9	–	40.5	65.0	34.7	48.4	34.1	78.7
11	43.9	58.8	44.1	–	55.5	29.5	55.0	41.5	33.0	47.4
12	38.0	54.7	43.8	–	66.5	47.0	48.5	59.7	41.0	38.9
13	54.8	40.1	42.3	–	49.0	37.0	41.8	29.3	29.8	30.9
14	41.2	25.0	35.0	–	38.1	36.8	26.3	26.9	37.9	22.7
15	33.9	29.8	43.1	–	41.9	29.0	35.0	25.9	39.8	35.9
16	34.2	20.6	34.5	–	35.2	29.9	29.1	27.2	25.4	25.0
17	27.2	34.8	38.6	–	24.7	38.9	25.0	25.2	23.2	25.8
18	21.8	34.6	37.6	–	24.8	27.4	26.8	21.6	20.2	25.8
19	30.7	25.7	32.0	–	26.0	22.4	31.2	17.7	20.3	24.0
20	24.7	25.3	24.7	–	54.4	23.4	28.3	27.3	26.5	20.0
21	30.6	24.8	33.4	–	34.1	29.5	33.4	26.1	28.7	25.5
22	28.0	29.0	36.6	–	16.1	26.3	33.7	20.9	23.5	24.2
23	22.9	28.5	40.0	–	19.8	27.3	20.7	24.3	28.9	35.0
24	25.8	38.8	42.4	–	26.9	26.9	25.6	19.7	32.7	33.9
25	39.3	40.1	39.4	–	19.8	60.6	29.9	33.3	54.0	32.4
26	38.8	43.0	28.9	–	21.9	37.8	28.8	23.5	27.5	33.3
27	56.2	31.4	45.5	–	28.9	32.9	22.3	22.7	23.7	32.3
28	60.7	33.0	32.5	–	31.5	35.4	26.4	32.9	31.8	33.5
29	60.2	34.4	33.8	–	21.3	26.9	30.0	39.7	33.2	30.5
30	63.2	25.3	31.1	–	23.8	56.0	29.3	27.1	24.0	40.5
31	68.5	30.6	34.5	–	31.3	42.3	25.4	22.9	29.1	21.3
32	42.2	42.5	35.4	–	20.7	35.2	21.2	16.1	21.9	23.9
33	46.9	37.0	34.6	–	34.3	33.9	32.1	29.6	35.5	30.8
34	33.6	32.6	40.6	–	26.4	32.4	34.4	35.4	27.4	26.0
35	48.0	38.9	44.0	–	36.1	28.4	24.5	26.0	32.3	29.3
36	26.8	33.7	36.2	–	34.1	29.4	26.4	22.0	45.1	28.4
37	53.6	39.9	35.1	–	44.4	46.6	30.3	37.8	16.9	44.6
38	33.2	31.2	40.8	–	47.9	31.1	25.0	44.4	24.3	26.6
39	68.5	39.4	29.9	–	32.7	32.2	32.1	32.3	30.7	31.7
40	–	55.1	41.2	–	28.4	23.9	42.0	37.9	25.0	18.9
41	–	51.2	–	–	36.9	16.6	39.0	40.8	30.1	21.9
42	37.8	73.6	–	–	28.1	57.4	59.2	30.7	35.5	35.7
43	67.5	48.5	–	–	74.1	82.2	71.4	42.5	62.4	39.8
44	108.4	93.1	–	–	70.5	63.7	79.3	35.8	62.1	64.0
45	67.1	104.0	–	–	79.6	80.9	74.7	36.8	89.7	44.7
46	182.9	50.7	–	–	158.0	70.6	78.1	45.3	42.6	79.5
47	185.5	177.1	–	–	95.0	61.0	53.1	61.9	73.6	42.1
48	114.2	79.7	–	–	198.2	67.4	74.2	63.7	109.6	34.4
49	302.9	140.2	–	–	109.7	40.7	64.9	73.5	55.5	85.8
50	169.9	226.6	–	–	87.6	31.2	44.2	94.1	69.8	106.8
51	296.3	68.1	–	75.4	61.6	148.7	179.9	163.9	120.3	199.8
52	63.0	156.3	–	35.1	107.1	93.5	171.0	215.8	49.0	57.2
Annually	79.1	73.8	55.5	55.2	61.2	52.2	50.0	49.2	48.1	50.1

Comparative analysis of daily concentration trends (2016 vs. 2025)

To further evaluate the long–term trends, a direct comparative analysis of daily PM_{10} concentrations was performed. While the heatmap analysis focuses on weekly aggregations, Figure 2 provides a higher–resolution comparison between the initial year of the study (2016) and the final year (2025) across a full 365–day cycle.

The daily time–series analysis confirms a substantial reduction in both the frequency and the magnitude of extreme pollution episodes. In 2016 (represented by the orange/red line), peak daily concentrations frequently exceeded 300 µg/m³. In contrast, the 2025 profile (blue line) exhibits a significant downward shift. Although the characteristic seasonal variability remains, the winter peaks in 2025 are approximately 40% lower than those recorded in 2016, indicating a significant decrease in the most severe pollution events over the analyzed decade.

A similar evaluation was conducted for the Karposh station, as shown in Figure 3. Although Karposh generally exhibits lower absolute PM_{10} concentrations compared to Lisiche, the relative improvement over the decade is even more pronounced. This station represents an urban environment with heavy traffic influence, making it a critical indicator for assessing urban mobility and general air quality management.

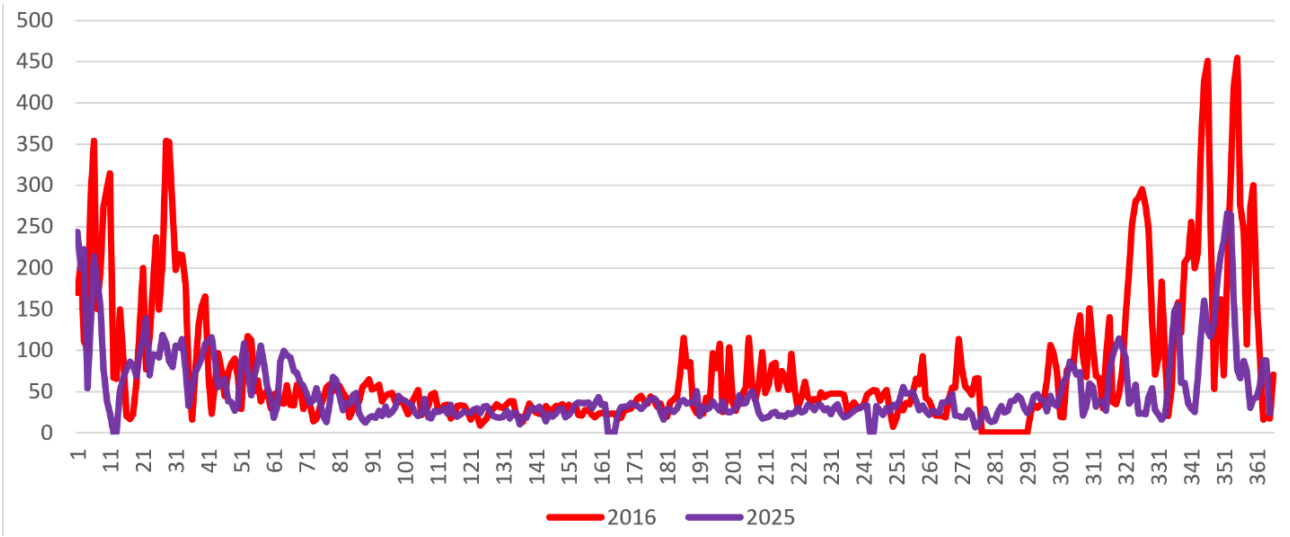

Fig. 2. Comparison of daily PM_{10} concentrations (µg/m³) at the Lisiche monitoring station for the years 2016 and 2025

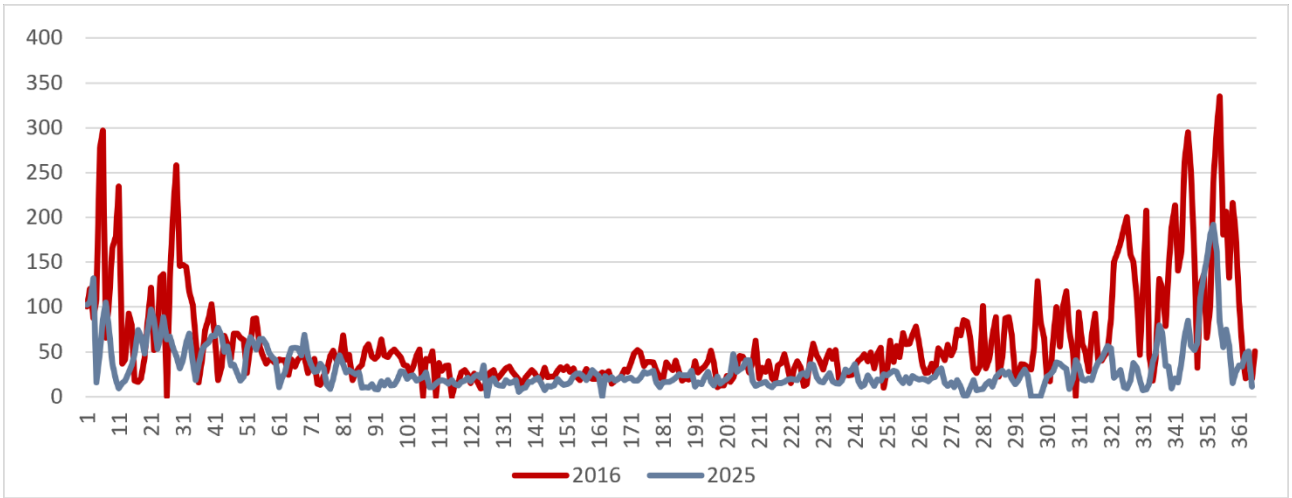

Fig. 3. Comparative analysis of daily PM_{10} concentrations at the Karposh monitoring station for the years 2016 and 2025

The daily trends for Karposh confirm a 48.3% reduction in annual average concentrations. As illustrated in the Figure, the extreme peaks that characterized the 2016 winter season are significantly flattened in the 2025 profile. The consistency of the summer concentrations across the decade suggests that baseline urban pollution remains stable, while the drastic winter reflect long–term changes in local emission dynamics. The fact that Karposh now stays more frequently within the regulatory daily limit of 50 µg/m³ compared to 2016 highlights the long–term evolution of air quality in this part of the city.

The overall progress in air quality management relative to statutory requirements is summarized in the annual trend analysis. Figure 4 illustrates the comparison of annual average PM_{10} concentrations for both the Karposh and Lisiche stations over the 2016–2025 period, measured against the European Union and national annual limit value.

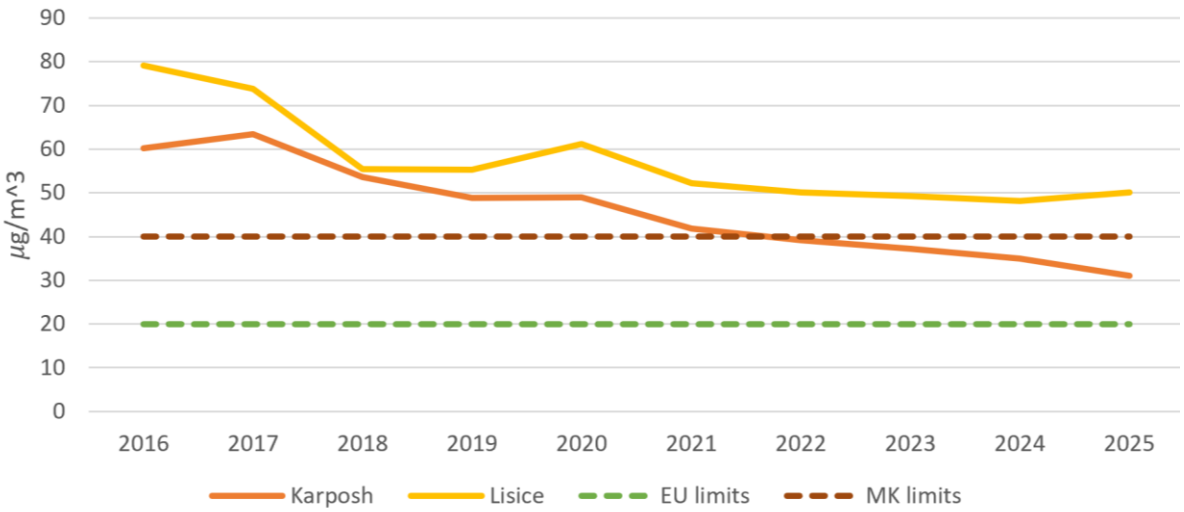

Fig . 4. Comparative analysis of annual average PM_{10} concentrations at Karposh and Lisiche stations (2016–2025)

As displayed in Figure 4, a consistent and measurable downward trend is evident for both monitoring locations. A significant milestone is reached at the Karposh station, where the annual average concentration successfully dropped below the regulatory threshold of 40 µg/m³ in the final stage of the analyzed decade.

The persistent gap between the two curves, despite the shared declining trend, highlights the localized impact of high–emission sources, particularly domestic heating in the Lisiche area. The alignment of both curves toward lower values suggests structural changes in emission profiles beyond seasonal meteorological variations.

Regulatory compliance: national legislation vs. EU frameworks

Despite the local improvements, the broader situation remains serious. According to the 2023 Global Air Quality Report [8] Macedonia still records significantly higher concentrations of PM2.5 compared to the average of the European Union countries. This data emphasizes the necessity of further systemic action. From a legal perspective, the results indicate that the existing air quality management system is limited in terms of its effectiveness. Although national legislation provides for obligations to prepare plans, their implementation does not always result in measurable improvements. In this context, the European approach, which introduces the right to compensation for health damages caused by illegal levels of air pollution, represents a significant step towards increasing the responsibility and protection of citizens.

To systematically contextualize these regulatory differences, Table 3 provides a comparative overview of the existing national legislative framework against the updated European Union directives regarding air quality standards and enforcement mechanisms.

Based on the parameters outlined in Table 3, this difference between the national and European approaches indicates a fundamental transformation in the concept of air quality management. While the national system is primarily based on planning and

administrative obligations without strict enforcement mechanisms, the European regulation introduces direct legal protection for citizens. With the introduction of the right to compensation for health impacts, air pollution is no longer treated solely as an environmental problem, but also as a fundamental human rights issue, which significantly increases the legal pressure on institutions for the effective implementation of measures.

Summarizing the findings, it is evident that achieving air quality targets in Skopje is closely linked to the strictness and enforcement of the regulatory framework. The comparative analysis between the national legislation and the new EU Directive 2024/2881 indicates a systemic gap in three key pillars: standards, accountability and transparency. While the Macedonian Regulation on Limit Values is a static document, the new EU regulation is a progressive act that fully incorporates the strictest WHO recommendations from 2021. Table 3 quantitatively illustrates this systemic gap regarding the fundamental standard for fine particulate matter ($PM_{2.5}$). As analyzed in the table, achieving alignment with the EU's 2030 target of 10 μg/m³ will require Macedonia to mandate a drastic 60% reduction from its current legally permissible annual limit of 25 μg/m³.

T a b l e 3

Comparative analysis of air quality management frameworks

Pollutants	Averaging period	MK decree (50/05, 04/13) μg/m³	Directive (EU) 2024/2881 (2030 Target) μg/m³	Percentage of reduction (EU ambition) %
$PM_{2.5}$ (Fine particles)	1 year	25	10	–60
PM_{10} (Suspended particles)	1 year	40	20	–50
PM_{10} (Suspended particles)	24 hours	50 (35 times a year)	45 (18 times a year)	Drastic reduction
NO_2 (Nitrogen dioxide)	1 year	40	20	–50
NO_2 (Nitrogen dioxide)	1 hour	200 (18 times a year)	200 (1 time per year)	Drastic reduction
NO_x (Nitrogen oxides)	1 year	30	30	0
SO_2 (Sulfur dioxide)	24 hours	125	50 μg/m³	–60
SO_2 (Sulfur dioxide)	1 hour	350 (24 times a year)	350 (1 time per year)	Drastic reduction

CONCLUSIONS

This study assessed long–term air quality management in Skopje by analyzing PM concentration trends over a ten–year period (2016–2025).

The analysis yields several specific conclusions:

- Significant decadal improvement: The Karposh station achieved a major milestone by successfully bringing the area into compliance with the EU annual limit value of 40 μg/m³, reflecting a nearly 50% reduction over the decade.
- Persistent residential hotspots: While Lisiche showed substantial reduction, it remains above the statutory threshold, confirming that residential areas heavily reliant on solid–fuel heating require more aggressive, localized interventions.
- Reduction in peak intensity: The comparative analysis of daily profiles between 2016 and 2025 indicates that the "pollution ceiling" has been lowered. Extreme winter peaks have decreased by approximately 40%, highlighting a significant shift in long–term pollution episodes, even though seasonal variability remains high.
- Methodological efficacy: Heatmap visualizations proved to be an indispensable tool for identifying spatiotemporal patterns that are often obscured in standard time–series graphs, specifically highlighting the interaction between emission cycles and the dynamics of the planetary boundary layer (PBL).

In conclusion, the integration of technical monitoring and legal analysis is a key step toward

improving air quality management. The study indicates that while Skopje is on a trajectory toward regulatory compliance, the winter months remain a challenge due to the complex interplay between emissions and stable atmospheric conditions. Future research should prioritize the integration of high–resolution meteorological models and urban parameters to enhance forecasting capabilities and refine the targeting of emission–reduction policies.

Acknowledgement: The authors would like to express their gratitude to the Faculty of Mechanical Engineering at Ss. Cyril and Methodius University in Skopje for providing the academic environment and necessary resources to conduct this research. Special acknowledgment is extended to the Ministry of Environment and Physical Planning (MOEPP) of Macedonia for providing the long–term air quality monitoring data from the Karposh and Lisiche stations, which was fundamental to the completion of this study.

REFERENCES

[1] World Health Organization (WHO) (2020): *Ambient (outdoor) air quality and health*, WHO website. https://www.who.int/news–room/fact–sheets/detail/ambient–(outdoor)–air–quality–and–health

[2] European Environment Agency (EEA) (2020): *Air quality in Europe – 2020 report*, EEA Report 0No 09/2020, https://www.eea.europa.eu/publications/air–quality–in–europe–2020–report

[3] Sanchez Martinez, G., Spadaro, J. V., Chapizanis, D., Kendrovski, V., Kochubovski, M., Mudu, P. (2018): Health impacts and economic costs of air pollution in the metropolitan area of Skopje, *International Journal of Environmental Research and Public Health*, vol. **15**, No. 4, pp. 626. https://doi.org/10.3390/ijerph15040626

[4] Andonova, E., Higueras Garcia, E., García–González, M. C. (2024): Air quality, health and the city: the case of Skopje, *International Urban Planning Research Seminar*. https://doi.org/10.5821/siiu.12768

[5] Dimitrovski, D., Markov, Z., Uler-Zefikj, M., Lazarevikj, M., Stojkovski, A. (2026): Numerical modelling of urban air pollution from residential heating: A case study of Skopje, *Atmosphere*, vol. **17**, No. 3, pp. 291. Available: https://www.researchgate.net/publication/402093005_Numerical_Modelling_of_Urban_Air_Pollution_from_Residential_Heating_A_Case_Study_of_Skopje

[6] Law on Ambient Air Quality, *Official Gazette of the Republic of Macedonia* No. 67/04, 92/07, 35/10, 47/11, 59/12, 100/12, 163/13, 10/15, 146/15, 151/21, and *Official Gazette of the Republic of North Macedonia* No. 156/24.

[7] European Parliament and Council (2024): Directive (EU) 2024/ 2881 on ambient air quality and cleaner air for Europe, *Official Journal of the European Union*, L 2024/2881. Available: https://eur–lex.europa.eu/eli/dir/2024/2881/oj

[8] IQAir.: *2023 World air quality report: Region and city $PM_{2.5}$ ranking*, iqair.com, Available: https://www.iqair.com/world–air–quality–report

Mechanical Engineering – Scientific Journal, Vol. **44,** No. 1, pp. 27–35 (2026)
Number of article: 702
Received: May 18, 2026
Accepted: June 22, 2026
In print: ISSN 1857–5293
On line: ISSN 1857–9191
UDC: 621.311.16:621.352
https://doi.org/10.55302/MESJ2644127gj

Review

THE ROLE OF RENEWABLE ENERGY SOURCES AND BATTERY ENERGY STORAGE SYSTEMS IN ENHANCING CRITICAL INFRASTRUCTURE RESILIENCE

Teodora Gjorgjievska[1], Simona Stamatoska[2], Nikola Manev[2], Tajana Kostadinova[3]

[1]*Institute for Security, Defense and Peace, Faculty of Philosophy, "Ss. Cyril and Methodius" in Skopje*
[2]Military Academy "General Mihailo Apostolski", Skopje,
associate member of Goce Delcev University, Stip
[3]*Faculty of Technology and Metalurgy, University of "Ss. Cyril and Methodius" in Skopje*
e-mail: nikola.manev@ugd.edu.mk

A b s t r a c t: The resilience of critical energy infrastructure has become an increasingly important component of national security, particularly in the context of growing energy demand, geopolitical uncertainty, and the ongoing transition toward renewable energy systems. In North Macedonia, the partial blackout of 18 May 2025 exposed vulnerabilities within the national power system when an overvoltage event resulted in the separation of the 400 kV and 110 kV networks and the loss of approximately 79% of the national electrical load. The event highlighted the potential consequences of infrastructure disruptions on the continuity of essential services and the functioning of society. This paper examines the role of renewable energy sources (RES) and battery energy storage systems (BESS) in enhancing the resilience of critical infrastructure. Using a resilience-based framework grounded in critical infrastructure protection principles, the study analyzes how decentralized renewable generation, energy storage technologies, and microgrid architectures can reduce vulnerability to technical failures, supply disruptions, and cascading effects within the electricity sector. In particular, emphasis is given to the contribution of solar photovoltaic systems, wind energy, and BESS in improving operational flexibility, supporting voltage and frequency stability, strengthening energy security, and enabling the continued operation of critical facilities during grid disturbances. The analysis demonstrates that the strategic integration of RES and BESS can enhance the robustness and adaptive capacity of critical energy infrastructure by reducing dependence on centralized generation and imported fossil fuels while increasing the ability of the power system to withstand and recover from disruptive events. The paper argues that renewable energy technologies and energy storage should be considered not only as instruments of decarbonization but also as key components of national resilience and critical infrastructure protection strategies.

Key words: energy security; critical infrastructure protection; distributed energy resources; microgrids; power system stability

УЛОГАТА НА ОБНОВЛИВИТЕ ИЗВОРИ НА ЕНЕРГИЈА И БАТЕРИСКИТЕ СКЛАДИШТА НА ЕЛЕКТРИЧНА ЕНЕРГИЈА ЗА ПОДОБРУВАЊЕ НА РЕЗИЛИЕНТНОСТА НА КРИТИЧНАТА ИНФРАСТРУКТУРА

А п с т р а к т: Резилиентноста на критичната енергетска инфраструктура станува сè поважна компонента на националната безбедност, особено во услови на зголемена побарувачка на енергија, геополитичка неизвесност и тековната транзиција кон обновливи извори на енергија. Во Северна Македонија делумниот прекин во снабдувањето со електрична енергија на 18 мај 2025 година ги откри ранливостите на националниот електроенергетски систем, кога појавата на пренапојување доведе до раздвојување на мрежите од 400 kV и 110 kV и губење на приближно 79% од целокупната покриеност со електрична енергија во државата. Настанот ги нагласи потенцијалните последици од нарушувањата на инфраструктурата врз континуитетот на основните услуги и функционирањето на општеството. Овој труд ја разгледува улогата на обновливите извори на енергија (ОИЕ) и на батериските складишта на електрична енергија (battery energy storage systems – BESS) во унапредувањето на резилиентноста на критичната инфраструктура. Користејќи рамка заснована на резилиентноста и принципите на заштита на критичната инфраструктура, истражувањето анализира како децентрализираното производство од обновливи извори, технологиите за складирање енергија и микро-мрежните архитектури можат да ја намалат ранливоста на технички дефекти, прекини во снабдувањето и каскадни ефекти во електроенергетскиот сектор и во целокупниот систем на критична инфраструктура. Посебен акцент е ставен на придонесот на фотоволтаичните системи, ветерната енергија и BESS во подобрувањето на оперативната флексибилност, поддршката на напонската и фреквенциската стабилност, зајакнувањето на енергетската безбедност и овозможувањето

непречено функционирање на критичните објекти при нарушувања во електроенергетската мрежа. Анализата покажува дека стратешката интеграција на ОИЕ и BESS може да ги зголеми робусноста и адаптивниот капацитет на критичната енергетска инфраструктура преку намалување на зависноста од централизирано производство и увоз на фосилни горива, истовремено зголемувајќи ја способноста на електроенергетскиот систем да издржи и побрзо да се поправи од нарушувањата. Трудот аргументира дека технологиите базирани на ОИЕ и системите за складирање енергија треба да се разгледуваат не само како инструменти за декарбонизација, туку и како клучни компоненти на националната резилиентност и суштински дел од стратегиите за заштита на критичната инфраструктура.

Клучни зборови: енергетска безбедност; заштита на критичната инфраструктура; дистрибуирани енергетски ресурси; микро-мрежи; стабилност на енергетскиот систем

1. INTRODUCTION

Critical energy infrastructure (CEI) comprising generation, transmission, distribution, and emerging storage systems represents a foundational pillar of national security in North Macedonia. It sustains essential societal functions, economic continuity, defense readiness, and public order. Any prolonged disruption can cascade into broader threats, including compromised military operations, halted industrial output, and erosion of public confidence. The National Security Strategy of the Republic of North Macedonia (2024 – 2029) explicitly identifies energy import dependency and vulnerabilities in critical infrastructure protection (particularly the energy sector) as priority risks requiring diversified and resilient solutions [1].

The partial blackout of 18 May 2025 vividly illustrates these vulnerabilities. At 04:59 CEST, overvoltage conditions during very low demand triggered cascading transformer trips, separating the 400 kV backbone from the 110 kV network and resulting in the loss of approximately 79 % of national load before MEPSO restored power within three hours [2]. Root causes included insufficient reactive power compensation, limited system flexibility, and reliance on centralized, import-dependent generation, factors that amplified the event's severity despite rapid recovery [2].

This incident is not isolated. A strikingly similar overvoltage-driven blackout struck the Iberian Peninsula on 28 April 2025, where voltage surges (exceeding absorption capacity) caused cascading generation disconnections, frequency collapse, and total system blackout across Spain and Portugal (lasting up to 10+ hours in areas), with ripple effects into southern France [3]. This event, the most severe in Europe in over two decades, underscores overvoltage as an emerging risk in modern grids, especially under low-load or high-renewable conditions [3, 4]. Lessons from the ongoing Russian invasion of Ukraine demonstrate how distributed solar generation and energy storage can enhance grid resilience and limit blackout propagation under targeted disruptions, providing a relevant model for strengthening infrastructure against hybrid threats [5].

Building on these insights, this paper posits that accelerated integration of renewable energy sources (RES), particularly utility-scale solar PV, wind, and co-located battery energy storage systems (BESS), function as a strategic facilitator of CEI resilience. Decentralized RES-based microgrids reduce single-point failure exposure, provide inherent local voltage/reactive support, enhance flexibility to counter intermittency and low-load instability, and diminish geopolitical risks tied to fossil fuel imports.

Recent momentum in North Macedonia further demonstrate the feasibility of this transition, including the 2026 Annual Plan for Construction of Energy Facilities approving 3 GW solar, 907 MW wind, and 2 GW/5 GWh storage capacity (total investment ≈€5.72 billion), as well as the 134 MWdc Bitola-3 solar project on reclaimed coal land (financed by EBRD and KfW, December 2025), expected to generate 180.9 GWh annually while avoiding approximately 134 kt of CO_2 emissions. These initiatives illustrate concrete pathways toward transforming legacy vulnerabilities of the national energy system into a more decentralized, flexible, and resilient infrastructure aligned with contemporary security and sustainability objectives [6-9]. Accordingly, this paper aims to evaluate how RES integration, supported by energy storage and microgrid configurations, can enhance the resilience of critical energy infrastructure under emerging grid stress conditions.

This paper is structured as a position paper that provides a narrative review of critical energy infrastructure resilience in North Macedonia. It first examines key resilience vulnerabilities, then analyzes lessons from the May 2025 blackout event, and finally reviews how renewable energy sources, energy storage systems, and decentralized architectures can contribute to improving critical energy infrastructure resilience.

Key definitions:

- *Critical Energy Infrastructure (CEI)* – Critical energy infrastructure refers to physical and cyber assets essential for the generation, transmission, distribution, and management of electricity whose disruption would significantly affect national security, economic stability, public safety, or essential services.
- *Resilience* – Resilience is the ability of an energy system to anticipate, withstand, adapt to, respond to, and recover from disruptive events while maintaining critical functionality.
- *Distributed Energy Resources (DERs)* – Distributed energy resources are small-scale generation, storage, and demand-side resources connected near the point of consumption.
- *Microgrids* – Microgrids are localized energy systems capable of operating either connected to the main grid or independently in islanded mode.
- *Battery Energy Storage Systems (BESS)* – Battery energy storage systems are electrochemical storage technologies capable of storing electricity and providing grid-support services such as frequency regulation, voltage support, peak shaving, and black-start capability.

2. CURRENT STATE OF THE ENERGY SECTOR

Threat landscape and vulnerabilities of North Macedonia's Energy CEI

The energy sector in North Macedonia constitutes critical energy infrastructure, essential for sustaining societal functions, economic activity, defense capabilities, and overall national security [10]. Disruptions to CEI can propagate rapidly, affecting public services, industrial output, and military readiness. The primary threats stem from a combination of geopolitical dependencies, technical fragilities, and emerging operational risks in a transitioning power system.

Geopolitical and import risks

North Macedonia remains heavily reliant on imported fossil fuels and electricity, exacerbating exposure to global price shocks, supply interruptions, and geopolitical pressures. In 2024 – 2025, fossil fuels (primarily coal and natural gas) accounted for approximately 58% of electricity generation [11]. Natural gas is sourced entirely through imports [12], while net electricity imports fluctuated significantly (e.g., 11.03% of gross consumption in 2024, down from higher levels in prior years due to domestic increases) [13]. This dependency on external suppliers for fossil fuels and occasional electricity creates chronic vulnerabilities: global energy market volatility (post-2022 Ukraine conflict spikes) directly translates to domestic price inflation and supply uncertainty [14]. The National Security Strategy (2024–2029) explicitly flags energy import dependency and lack of diverse energy supplies as key risks, noting that reliance on fossil fuels heightens susceptibility to external shocks and secondary crises [1].

Recent geopolitical developments, particularly tensions involving the United States, Israel, and Iran in early 2026, further highlight the fragility of global energy markets. Military escalation and strategic uncertainty contributed to significant oil price volatility, driven by both actual and anticipated disruptions. The risk of restricted access to critical chokepoints such as the Strait of Hormuz, through which approximately 20% of global oil flows transit, introduced a substantial geopolitical risk premium, leading to sharp price increases and heightened uncertainty in global energy markets [15, 16]. Even in cases where supply disruptions were temporary or avoided, price fluctuations remained pronounced, reflecting the sensitivity of energy markets to geopolitical instability. For import-dependent countries such as North Macedonia, these dynamics translate directly into increased fuel prices, inflationary pressures, and exposure to cascading economic shocks, reinforcing the risk of broader energy and security crises.

Technical vulnerabilities

North Macedonia's CEI suffers from ageing infrastructure, inadequate reactive power management, and instability under low-load conditions. The transmission system (400 kV and 110 kV network) is characterized by ageing infrastructure, with a significant portion of equipment approaching or exceeding its designed operational lifetime, limiting both efficiency and operational flexibility [17, 18]. This structural constraint reduces the system's ability to maintain stable voltage profiles under dynamic operating conditions and increases reliance on external support during contingencies.

In addition, the system exhibits limited reactive power compensation capability due to insufficient deployment of modern voltage control technologies, such as shunt reactors, static VAR compensators (SVCs), and STATCOM devices [18]. As highlighted in European system operation guidelines, such technologies are essential for maintaining voltage stability in transmission networks with variable load profiles and high interconnection levels. Their absence or limited penetration in North Macedonia's grid reduces the system's capacity for dynamic voltage regulation and increases sensitivity to disturbances [19].

Under low-load or light-loading conditions, the system is particularly vulnerable to voltage instability. Long transmission lines operating at reduced load generate significant capacitive reactive power, which can lead to voltage rise phenomena across the network. In the absence of adequate reactive power absorption equipment, this surplus reactive power cannot be properly compensated, resulting in voltage excursions beyond acceptable operational limits [20]. These effects are further amplified by interconnections with neighboring systems, where power flows and voltage conditions may vary, introducing additional complexity into local voltage control.

Overall, the combination of ageing infrastructure, limited reactive power compensation, and inherent capacitive effects in lightly loaded transmission lines creates persistent operational challenges for the stability of North Macedonia's electricity system, particularly during periods of low demand and high system interconnectivity.

The 18 May 2025 blackout

The partial blackout on 18 May 2025 exemplifies how these vulnerabilities converge into high-impact events. At 04:59 CEST, during very low predawn demand and minimal cross-border flows, overvoltage conditions escalated on the 400 kV network. Lightly loaded lines generated excess capacitive reactive power, pushing voltages toward 450 kV in the absence of online reactors, SVCs, or STATCOMs [2]. Cascading trips of 400/110 kV transformers (triggered by overvoltage protection) progressively isolated the 110 kV network, resulting in a full blackout across that subsystem and loss of approximately 79% of national load [2]. The 400 kV backbone remained intact, enabling faster restoration by MEPSO, which completed reconnection in 3 hours.

While recovery was relatively fast, the incident exposed a significant system fragility: a localized disturbance propagated into widespread load shedding, disrupting essential services and exposing gaps in reactive power planning and low-load forecasting. Classified as ICS Scale 3 (highest severity) by the European Network of Transmission System Operators for Electricity (ENTSO-E), the event underscores increasing risks in systems transitioning toward variable and low-load operation [2, 17, 18].

Broader security implications

The National Security Strategy (2024–2029) identifies energy import dependency and CI vulnerability as explicit national security risks, warning that weak protection of energy infrastructure threatens disruption of essential services, stability, and resilience [1, 21]. Lack of a dedicated critical infrastructure law (defining responsibilities, funding, standards, and training) compounds these issues, as does insufficient focus on cyber-physical interdependencies [10]. In a hybrid threat environment, such vulnerabilities could be exploited through sabotage, cyberattacks, or supply coercion, with cascading effects on defense and societal functions [22].

Beyond these direct operational risks, vulnerabilities in CEI also have broader systemic security implications due to the increasing interdependence between energy infrastructure and other critical sectors. Modern energy systems are tightly coupled with digital communication networks, transport systems, healthcare services, and defense command-and-control structures. As a result, disturbances in the power sector can rapidly propagate across multiple domains, transforming localized technical failures into systemic national-level disruptions. For North Macedonia, where redundancy and distributed backup capabilities remain limited, even short-duration outages may compromise emergency response coordination, border management systems, and operational readiness of security institutions. This interconnectivity amplifies the strategic relevance of CEI protection, positioning energy system resilience as a foundational component of overall national resilience under both conventional and hybrid threat conditions.

To illustrate the spectrum of threats, Figure.1 presents a simple threat matrix classifying risks by probability and impact. The matrix highlights the need for resilience measures that address both rare catastrophic events (via distributed generation and

storage) and persistent chronic pressures (diversification to reduce import exposure). These vulnerabilities collectively undermine CEI resilience and national security.

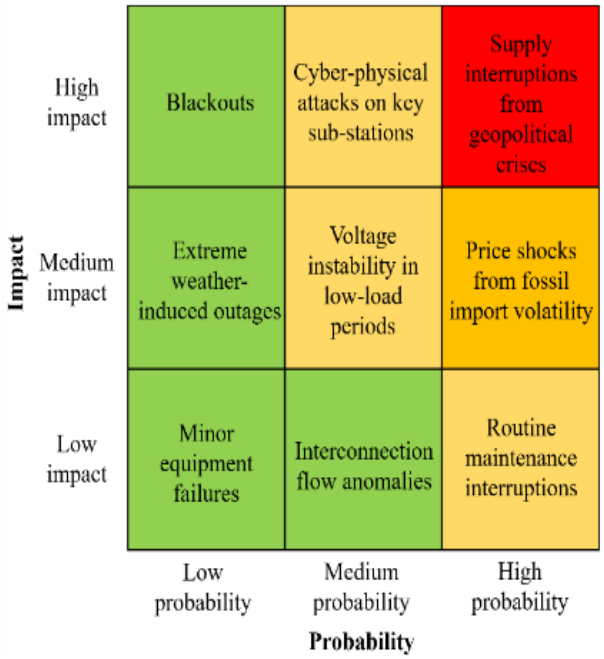

Fig. 1. Critical energy infrastructure risk matrix

3. RENEWABLES INTEGRATION AS A RESILIENCE FACILITATOR

The vulnerabilities outlined in the previous section like geopolitical import dependency, ageing grid assets, reactive power deficiencies, and low-load instability, can be materially mitigated by strategic integration of RES, particularly utility-scale solar photovoltaic (PV), wind power, and co-located BESS. Rather than viewing RES solely as a decarbonization tool, this paper positions accelerated RES deployment as a core facilitator of CEI resilience, transforming centralized, import-reliant systems into more decentralized, flexible, and autonomous architectures.

As shown in Figure 2, resilience improvements associated with renewable energy integration extend beyond the generation mix itself and affect multiple operational and structural dimensions of the power system. Conventional centralized systems are characterized by concentrated generation assets, high import dependence, slower recovery processes, limited operational flexibility, and greater vulnerability to cascading failures. In contrast, renewable-integrated decentralized systems benefit from distributed generation, inverter-based voltage support, enhanced recovery capabilities enabled by BESS, and reduced exposure to geopolitical supply risks. The figure further illustrates how decentralized architectures support island-capable microgrids, improve continuity for critical facilities, and provide greater scalability through modular deployment.

These attributes collectively strengthen the ability of the energy system to withstand, absorb, adapt to, and recover from disruptive events.

Decentralization and reduced single-point failure risks

The integration of renewable energy sources (RES) fundamentally transforms the structural topology of the power system from a highly centralized configuration toward a distributed generation model. In conventional energy systems, electricity production is concentrated in large thermal or hydro plants, connected through a limited number of high-voltage transmission corridors. This architecture inherently introduces single-point failure risks, where disturbances affecting key nodes can propagate rapidly across the entire system, potentially resulting in cascading outages.

In contrast, distributed renewable generation, particularly solar photovoltaic (PV) and wind installations enables geographical dispersion of generation assets. This decentralization reduces dependency on individual generation units and transmission corridors, thereby limiting the spatial extent of failure propagation. In the context of North Macedonia, where the 18 May 2025 blackout demonstrated how localized overvoltage conditions can escalate into system-wide load loss, decentralization provides a structural mitigation mechanism against similar cascading events.

When combined with distributed energy resources (DERs), renewable systems can also segment the grid into semi-independent operational zones (microgrids), further reducing systemic vulnerability. This structural shift is particularly relevant for critical facilities such as hospitals, military bases, and emergency response centres, which can maintain localized operation even under wider grid disturbances.

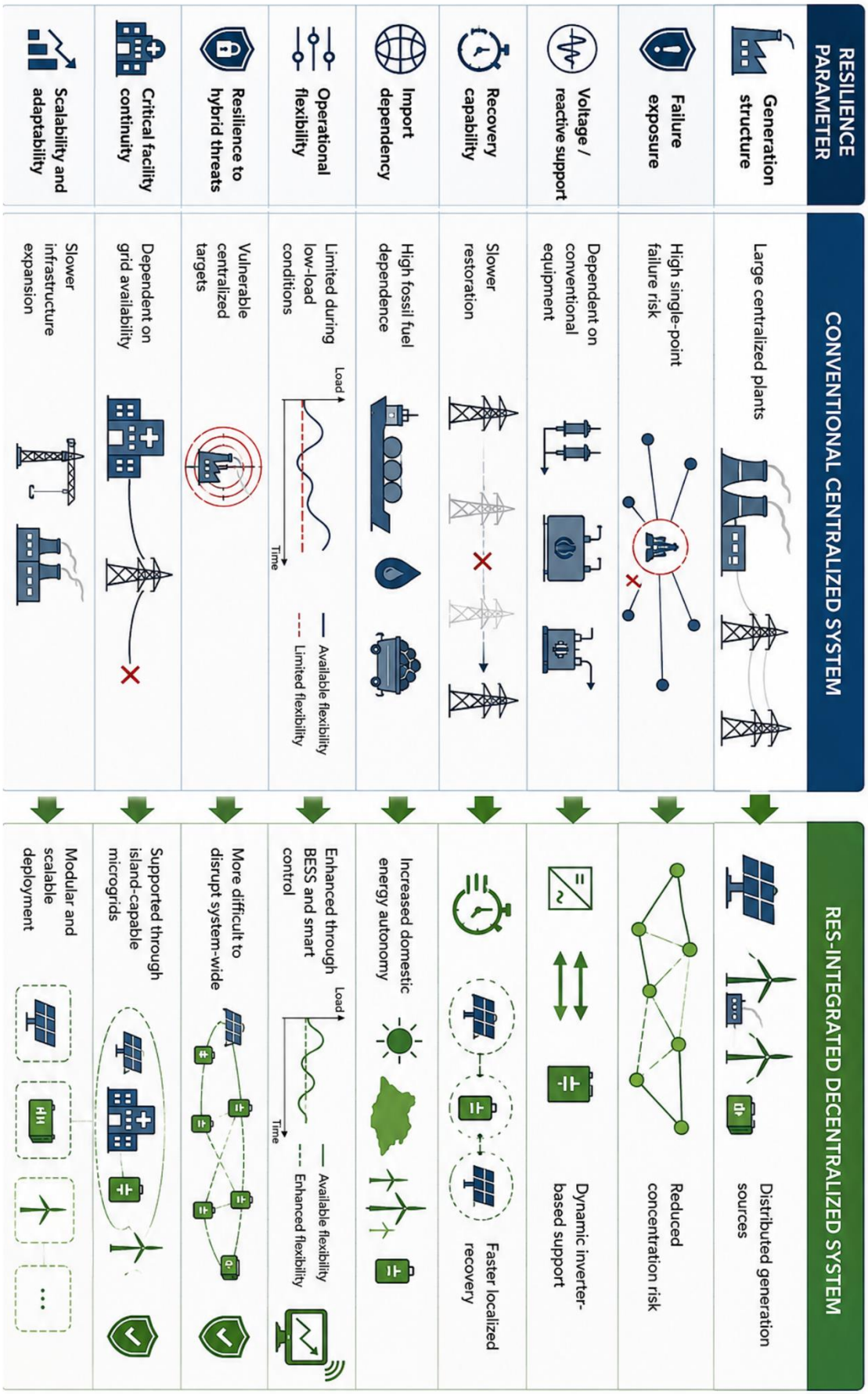

Fig. 2. Comparative resilience characteristics of centralized vs decentralized energy systems

Flexibility and voltage/reactive power support

A key technical limitation of North Macedonia's existing energy system is insufficient operational flexibility, particularly under low-load conditions where voltage instability becomes more pronounced. Renewable energy systems, when integrated with modern power electronics and energy storage, can significantly improve system flexibility and dynamic stability. Unlike conventional synchronous generators, inverter-based renewable systems can be configured to provide fast reactive power compensation. Through advanced control algorithms, PV and wind inverters, as well as battery energy storage systems (BESS), can actively support voltage regulation by absorbing or injecting reactive power as needed. This capability is particularly important in scenarios characterized by excess capacitive reactive power, such as lightly loaded transmission lines, which contributed to the 2025 blackout event.

Battery storage systems further enhance flexibility by providing multiple grid-support functions [23], including:

- fast frequency response,
- voltage stabilization,
- peak shaving,
- spinning reserve substitution,
- and black-start capability.

These features allow the system to respond more effectively to rapid changes in demand or generation, reducing the likelihood of voltage collapse or cascading disconnections. In this sense, RES combined with BESS transitions from being a passive generation source to an active stability component of the grid.

Geopolitical risk reduction and energy autonomy

North Macedonia's current energy mix is characterized by significant dependence on imported fossil fuels and external electricity markets. This structural dependency exposes the system to geopolitical risks, global price volatility, and supply chain disruptions. As demonstrated during recent international energy crises and regional conflicts, external shocks can rapidly translate into domestic economic and energy instability. The integration of renewable energy sources directly reduces this exposure by increasing the share of domestically produced energy. Solar and wind resources, unlike fossil fuels, are locally available and not subject to international supply chain constraints or geopolitical bottlenecks such as transit routes and chokepoints. This contributes to improved energy sovereignty and reduced strategic vulnerability. In addition, distributed renewable systems reduce reliance on fuel logistics and import infrastructure, which are often the first targets of disruption in hybrid or conflict-related scenarios. From a national security perspective, this shift enhances strategic autonomy, ensuring that essential services are less exposed to external coercion or supply interruptions.

Overall resilience benefits of RES integration

When considered collectively, the integration of renewable energy sources, energy storage systems, and decentralized grid architectures significantly enhances the resilience profile of critical energy infrastructure. The combined effect of decentralization, operational flexibility, and reduced external dependency results in a more adaptive and robust energy system (Table 1).

Table 1

Vulnerability–resilience summary

Vulnerability	Consequence	Resilience measure	Supporting technology
Import dependency	Supply disruption	Domestic RES deployment	Solar PV, Wind
Low-load overvoltage	Voltage instability	Reactive power control	Smart inverters, STATCOM
Limited flexibility	Poor disturbance response	Flexible operation	BESS
Critical facility exposure	Service interruption	Island-capable microgrids	DERs + BESS
Slow restoration	Extended outages	Black-start capability	BESS
Centralized generation	Cascading failures	Distributed generation	RES + DERs
Ageing grid assets	Reliability degradation	Smart-grid modernization	Digital monitoring

Key resilience improvements include:

- distributed generation to reduce the risk of cascading failures,
- improved voltage and frequency stability via inverter-based control systems,
- faster recovery and system restoration through localized operation and black-start capability,
- enhanced continuity of critical services through microgrid islanding,
- and reduced exposure to geopolitical and fuel supply shocks.

However, it is important to emphasize that RES integration alone is not sufficient. Renewable energy deployment should therefore be viewed as one component of a broader resilience strategy rather than a standalone solution. Without adequate storage, grid modernization, advanced forecasting, reactive power management, cybersecurity protection, and institutional coordination, high penetrations of variable renewable generation may introduce new operational challenges, including voltage fluctuations, congestion, and balancing difficulties. Its resilience benefits are maximized only when supported by complementary investments in smart grid technologies, advanced monitoring and forecasting systems, reactive power compensation infrastructure, and cybersecurity frameworks. Without these supporting systems, high penetration of variable renewable energy may introduce new operational challenges.

4. CONCLUSION

The findings presented in this paper demonstrate that North Macedonia's ongoing energy transition represents both a strategic opportunity and an emerging resilience challenge for critical energy infrastructure. While the country has accelerated the integration of renewable energy sources through ambitious solar, wind, and energy storage projects aligned with broader European decarbonization objectives, the institutional, legislative, and technical frameworks required to fully support this transition remain underdeveloped. Existing gaps in critical infrastructure protection policy, reactive power management, grid modernization, and coordinated resilience planning increase the risk that rapid renewable integration may outpace the operational capabilities of the national energy system.

The 18 May 2025 partial blackout highlighted how structural weaknesses within the transmission network, including ageing infrastructure, insufficient reactive power compensation, and limited flexibility under low-load conditions, can rapidly escalate into large-scale disruptions. At the same time, the event demonstrated the urgent need for resilience-oriented modernization strategies capable of addressing both conventional technical vulnerabilities and emerging hybrid threats.

This paper argues that renewable energy integration should therefore be approached not solely as a decarbonization objective, but as part of a broader resilience and national security strategy. Distributed renewable generation, battery energy storage systems, and microgrid architectures have the potential to significantly enhance system adaptability, reduce single-point failure exposure, improve voltage and frequency support, and strengthen continuity of operations for critical facilities. However, these benefits can only be fully realized through the parallel development of adequate legislative frameworks, modern grid management capabilities, smart-grid technologies, cybersecurity protections, and resilience-focused operational planning.

Rather than eliminating vulnerabilities automatically, the transition toward decentralized renewable systems redistributes and transforms risk across the energy sector. Consequently, the resilience of future renewable-based systems will depend not only on installed generation capacity, but also on the ability of institutions, regulators, and system operators to anticipate, manage, and mitigate the new operational complexities associated with high renewable penetration.

For North Macedonia, the planned expansion of solar, wind, and storage capacity represents a unique opportunity to simultaneously advance energy security, sustainability, and national resilience. Yet achieving these objectives will require a more comprehensive strategic approach that integrates renewable deployment with critical infrastructure protection principles, legislative modernization, and long-term system flexibility planning. In this sense, the energy transition should not be viewed as a purely environmental process, but as a multidimensional transformation directly linked to national security, economic stability, and societal resilience under increasingly complex geopolitical and technological conditions.

REFERENCES

[1] Government of the Republic of North Macedonia (2024): *National Security Strategy of the Republic of North Macedonia (2024–2029,* Skopje.

[2] ENTSO-E (2025a): *Factual Report on the Grid Incident in North Macedonia on 18 May 2025*. Brussels, November 2025. Available at: https://eepublicdownloads.blob.core.windows.net/public-cdn-container/clean-documents/Publications/2025/251106_factual_report_on_MEPSO_incident_18_May_2025.pdf

[3] ENTSO-E (2025b): *Factual Report on the Grid Incident in Spain and Portugal on 28 April 2025*. Brussels, October 2025.

[4] Morão, H. (2026): The 2025 Iberian Peninsula blackout: Lessons for modern power systems and policy implications. *Utilities Policy*. Vol. **101**. https://doi.org/10.1016/j.jup.2026.102196

[5] Manev, N., Nikolov, E. (2022). The European green deal and EU's energy transition in the wake of the War in Ukraine. *Contemporary Macedonian Defence*. **43** (XXII), pp. 37–45.

[6] Ministry of Energy (2026): *Annual Plan for the Construction of Energy Facilities for 2026*. Ministry of Energy, Mining and Mineral Resources of the Republic of North Macedonia, Skopje.

[7] Balkan Green Energy News (2026): *North Macedonia unveils EUR 5.7 billion plan for new power plants, energy storage*. https://balkangreenenergynews.com/north-macedonia-unveils-eur-5-7-billion-plan-for-new-power-plants-energy-storage

[8] EBRD (2025): EBRD and KfW bolster North Macedonia's green transition: €87 million financing for Bitola 3 solar plant. https://www.ebrd.com/home/news-and-events/news/2025/ebrd-and-kfw-bolster-north-macedonia-s-green-transition.html

[9] PV Magazine (2025): Financing secured for 134 MW solar project in North Macedonia. https://www.pv-magazine.com/2025/12/23/financing-secured-for-134-mw-solar-project-in-north-macedonia

[10] Ministry of Defense (2022): *Draft Law on Critical Infrastructure*. Available: https://ener.gov.mk/Default.aspx?item=pub_regulation&subitem=view_reg_detail&itemid=77229

[11] State Statistical Office of the Republic of North Macedonia (2025): *Energy Balance of the Republic of North Macedonia*, 2024. Skopje.

[12] IEA (2023): *Natural Gas Information: North Macedonia Country Notes*. International Energy Agency. Paris, Available at: https://www.iea.org/countries/north-macedonia/natural-gas

[13] ENTSO-E (2024): *Statistical Factsheet and Electricity Exchange Data. European Network of Transmission System Operators for Electricity*. Brussels. Available at: https://www.entsoe.eu

[14] World Bank (2023): *The Global Impact of the War in Ukraine on Energy and Food Markets*. Washington, DC. Available at: https://www.worldbank.org/en/topic/energy/publication/global-impact-of-war-in-ukraine-on-energy-and-food-markets

[15] EIA (2025): *World Oil Transit Chokepoints*. U.S. Energy Information Administration (EIA). Washington, DC.

[16] Reuters (2026): *The Iran war has shattered oil's price compass*. April 16, 2026. Available at: https://www.reuters.com/markets/commodities/iran-war-has-shattered-oils-price-compass-2026-04-16/

[17] Regulatory Commission (2025): *Annual Report 2024. Energy, Water Services and Municipal Waste Management. Services Regulatory Commission of the Republic of North Macedonia. Skopje*. Available at: https://www.erc.org.mk/page_en.aspx?id=342

[18] MEPSO (2024): Ten-Year Network Development Plan 2025–2035. Skopje, 2024. Available at: https://www.mepso.com.mk/docs/Plan%20za%20razvoj%20na%20elektroprenosniot%20sistem%20za%20period%202025%20-%202035_22012025.pdf

[19] Pehchevski, D. (2026): *The Weakest Link: Towards a Transmission Grid that Supports Decarbonisation in the Western Balkans*. Available at: https://bankwatch.org/wp-content/uploads/2026/02/2026_02_The-weakest-link_Towards-a-transmission-grid-that-supports-decarbonisation-in-the-Western-Balkans.pdf

[20] Wood, A. J., Wollenberg, B. F. (2013*): Power Generation, Operation, and Control*, 3rd ed., Wiley.

[21] Manev, N., Jovanovikj, E., Dimitrovski. D. (2024): Review of the required legislative changes to facilitate N. Macedonia's transition to renewables. *Mechanical Engineering – Scientific Journal*. Vol. **42**, No. 2, pp. 117–125. https://doi.org/10.55302/MESJ24422117m

[22] Gjorgjievska, T. (2026): Assessing the vulnerabilities of critical infrastructure in the age of hybrid threats. S*ecurity Dialogues*. **16** (2), pp. 33. https://doi.org/10.47054/SD25233gj

[23] Dimitrovski, D., Manev, N., Jovanovikj, E., Uler-Zefik, M. (2022): Repurposed EV batteries integration in smart energy grids to facilitate a greener energy sector. *Proceedings of the ICIST 12 Conference in Kopaonik, Serbia.*

Mechanical Engineering – Scientific Journal, Vol. **44,** No. 1, pp. 37–45 (2026)
Number of article: 703
Received: May 10, 2026
Accepted: June 14, 2026
In print: ISSN 1857–5293
On line: ISSN 1857–9191
UDC: 004.771-047.36:[502.3:613.15]
https://doi.org/10.55302/MESJ2644137dm

Original scientific paper

DESIGN AND DEVELOPMENT OF A LOW-COST ENVIRONMENTAL MONITORING SYSTEM FOR UNIVERSITY CAMPUS APPLICATIONS

Simona Domazetovska Markovska, Evgenija Jovanovska, Mario Angjelkovski, Mila Spiroska, Danimir Pavlovski, Ivan Tanasoski

Faculty of Mechanical Engineering, "Ss. Cyril and Methodius" University in Skopje, P.O. Box 464, MK-1001 Skopje, Republic of North Macedonia
simona.domazetovska@mf.edu.mk

A b s t r a c t: This paper presents the design and framework development of a low-cost IoT-based multi-parameter air quality monitoring network for smart campus applications, including its hardware and software architecture and an initial evaluation of the proposed prototype. The proposed system is designed to measure key environmental parameters, including particulate matter (PM_1, $PM_{2.5}$, PM_{10}), ambient noise levels (dB), temperature and barometric pressure. The system is based on cost-effective hardware components and integrates wireless communication technologies to enable real-time data transmission. The system enables continuous monitoring while remaining user-friendly and easy to deploy. Unlike traditional monitoring systems, which rely on large and expensive equipment installed at fixed locations, the proposed system is compact and portable, allowing deployment across different locations and enabling users to monitor environmental conditions in real time, while also providing indicative insights into potential changes in measured levels. Experimental validation of the noise sensing module demonstrated good agreement with a reference sound level meter, indicating the suitability of the proposed system for indicative environmental monitoring applications.

Key words: IoT; air quality monitoring; environmental monitoring; low-cost system; wireless communication

ДИЗАЈН И РАЗВОЈ НА НИСКОБУЏЕТЕН СИСТЕМ ЗА МОНИТОРИНГ НА ЖИВОТНАТА СРЕДИНА ЗА АПЛИКАЦИИ НА УНИВЕРЗИТЕТСКИТЕ КАМПУСИ

А п с т р а к т: Во овој труд е претставен дизајнот и развојната рамка на нискобуџетна мрежа базирана на IoT за мониторинг на повеќе параметри на квалитетот на воздухот, наменета за примена во паметен кампус, вклучувајќи ја нејзината хардверска и софтверска архитектура, како и почетна евалуација на предложениот прототип. Предложениот систем е дизајниран за мерење на клучни параметри од животната средина, вклучувајќи суспендирани честички (PM_1, $PM_{2.5}$, PM_{10}), нивоа на амбиентална бучава (dB), температура и атмосферски притисок. Системот се базира на економични хардверски компоненти и интегрира безжични комуникациски технологии со цел да се овозможи пренос на податоци во реално време. Системот овозможува континуиран мониторинг, при што останува едноставен за користење и лесен за поставување. За разлика од традиционалните мониторинг-системи, кои се базираат на голема и скапа опрема инсталирана на фиксни локации, предложениот систем е компактен и преносliв, што овозможува негово поставување на различни локации и следење на условите во животната средина во реално време, како и добивање индикативни согледувања за можни промени на измерените вредности. Експерименталната валидација на модулот за мерење бучава покажа добро совпаѓање со референтен мерач на ниво на звук, што укажува на соодветноста на предложениот систем за индикативни апликации за мониторинг на животната средина.

Клучни зборови: IoTM; мониторинг на квалитет на воздух; мониторинг на животна средина; нискобуџетен систем; безжична комуникација

INTRODUCTION

Air pollution represents one of the major environmental challenges today, with significant impacts on human health, contributing to approximately 7 million premature deaths annually and being closely linked to respiratory and cardiovascular diseases. Skopje is frequently ranked among the most polluted cities in Europe, particularly during the winter season, when elevated concentrations of particulate matter ($PM_{2.5}$) lead to unhealthy air quality levels [1]. These conditions are mainly caused by residential heating, traffic emissions, industrial activities, and unfavorable valley topography.

Motivated by these challenges, this work presents the development of a low-cost IoT-based system for real-time monitoring of environmental parameters and air quality. The proposed system consists of an autonomous sensing unit equipped with sensors for measuring particulate matter ($PM_{2.5}$ and PM_{10}), ambient temperature, and environmental noise levels. The collected data are transmitted via LoRaWAN to a central gateway and further forwarded to a cloud-based platform for real-time visualization and analysis. The system enables continuous monitoring with periodic measurements and supports historical data analysis through graphical representations. The rapid development of IoT technologies enables cost-effective real-time monitoring and integration of multiple sensing units, contributing to more accurate environmental assessment and improved decision-making in urban environments. Several studies have proposed IoT-based environmental monitoring systems. In the study [2], a low-cost system based on Arduino UNO is presented, capable of measuring multiple environmental parameters; however, it lacks scalability and long-range communication capabilities. Similarly, [3] introduces a solar-powered system using ESP8266 and Wi-Fi communication, which is energy-efficient but limited by short-range connectivity. In [4], an ESP32-based system is proposed for real-time monitoring, but it is primarily designed for localized applications and depends on Wi-Fi communication.

In contrast, the system proposed in this work utilizes LoRaWAN communication, enabling low power, long-range data transmission suitable for distributed deployment across smart campus and urban environments. Additionally, the solution emphasizes a compact and scalable design with real time monitoring and historical data analysis capabilities.

CONCEPT FOR SENSOR NETWORK AT THE FACULTY

Proposed sensor deployment across the faculty campus

The concept of the proposed sensor network is based on the deployment of multiple distributed measurement units across our faculty campus, with the primary objective of capturing spatial variations in environmental conditions (Figure 1).

Fig. 1. Campus deployment concept of the IoT environmental monitoring system

The placement of the units is proposed based on the functional characteristics of the campus environment. Measurement units are intended to be installed at building entrances, courtyard areas, laboratory surroundings, and parking zones, where variations in air quality are expected due to human activity and localized emission sources. As a conceptual implementation, the units are proposed to be mounted on existing infrastructure elements, such as lighting poles (lamp posts), at a height of approximately 2.5 to 3 meters above ground level.

This proposed installation height is selected to approximate the human breathing zone while reducing the influence of ground level disturbances and ensuring unobstructed airflow around the sensors.

System Architecture

The system architecture is designed as a modular and distributed structure consisting of sensing, processing, communication, and visualization layers. The architecture enables continuous acquisition, preprocessing, and transmission of environmental data within a smart campus framework. The black-box model in Figure 2 illustrates the system as a functional unit that converts environmental inputs into processed and transmitted information. Inputs include ambient air parameters, electrical energy, and control signals, while outputs consist of measured data, visualized information, and transmitted signals via LoRa. The system performs acquisition, preprocessing, and communication of environmental parameters.

The functional architecture of the proposed system is illustrated in Figure 3, where the overall process is decomposed into several interconnected subsystems responsible for sensing, data acquisition, processing, communication, and visualization.

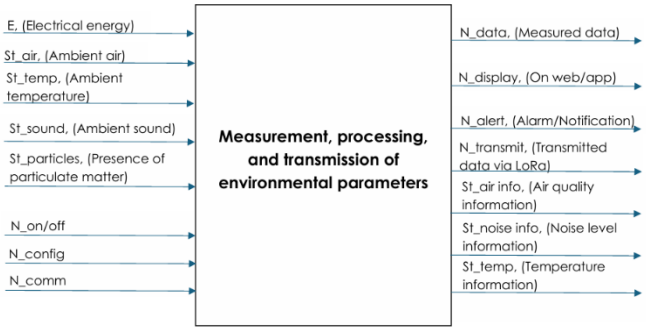

Fig. 2. Black-box model of the IoT environmental monitoring system

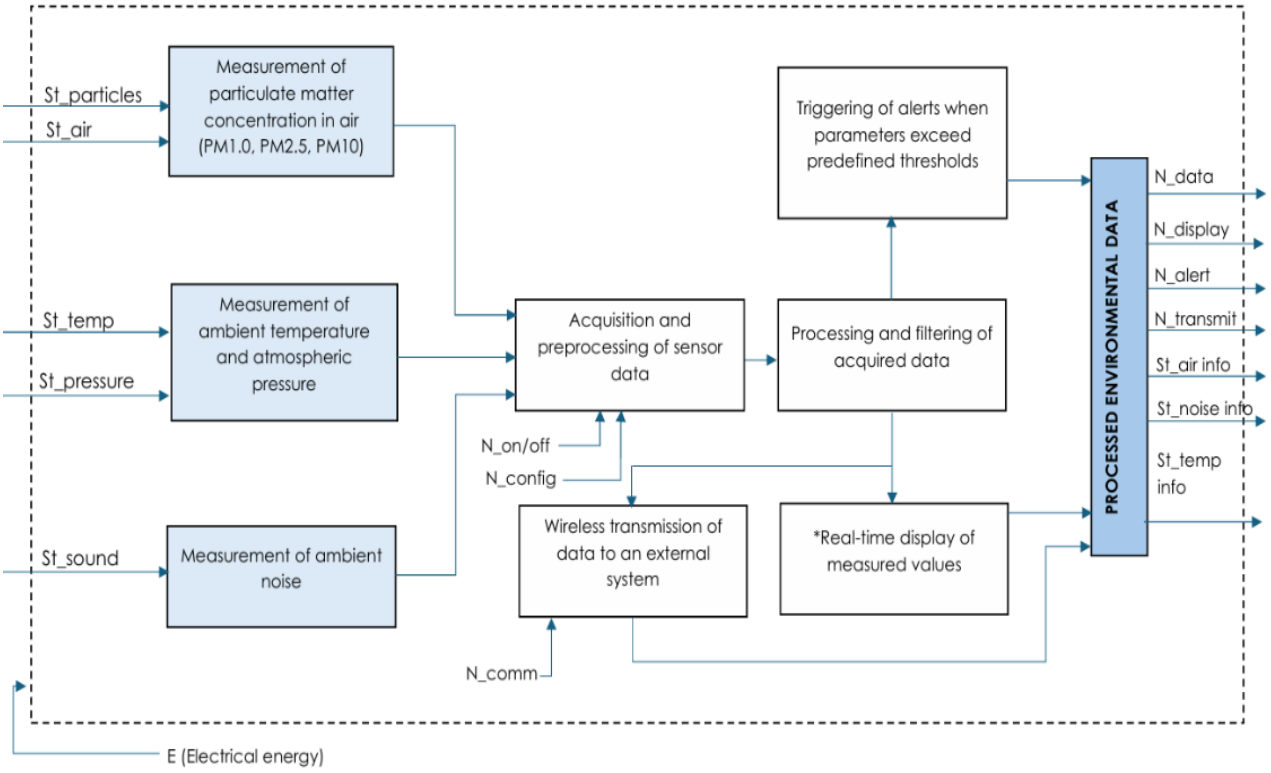

Fig. 3. Functional block diagram of the environmental monitoring system

The system begins with the sensing stage, where environmental parameters are continuously measured. This includes particulate matter concentration ($PM_{1.0}$, $PM_{2.5}$, PM_{10}), ambient temperature, atmospheric pressure, and environmental noise. These measurements represent the primary input signals to the system. The acquired sensor data are forwarded to the data acquisition and preprocessing block, where initial operations such as signal conditioning, synchronization, and formatting are performed.

Control inputs such as system configuration, communication settings, and on/off states are also processed at this stage. Following preprocessing, the data are subjected to further processing and filtering in order to improve measurement reliability and remove potential noise or outliers (Figure 4).

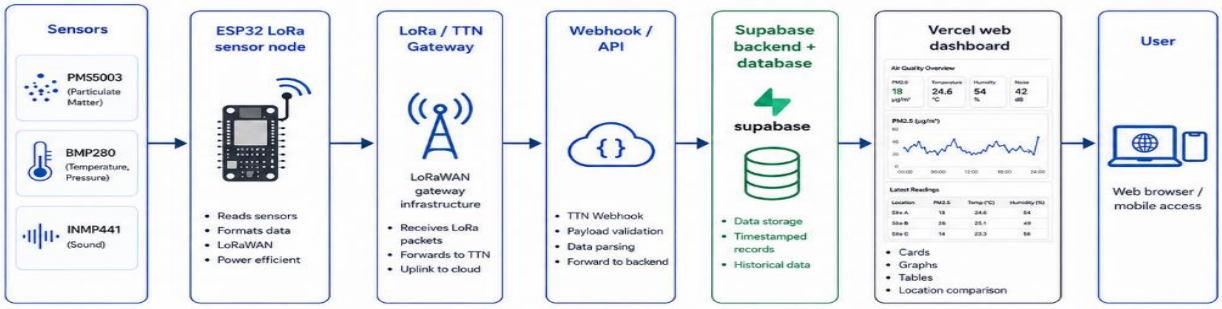

Fig. 4. Data transmission and visualization architecture using Supabase and Vercel

Based on the processed values, the system can trigger alerts when predefined threshold limits are exceeded. The processed environmental data are then directed toward two main outputs. The first output includes real-time visualization of measured values through display interfaces such as web or mobile applications. The second output involves wireless transmission of data to an external system using LoRa communication.

This modular structure enables efficient data flow, scalability, and reliable operation of the system within a distributed environmental monitoring network (Figure 5).

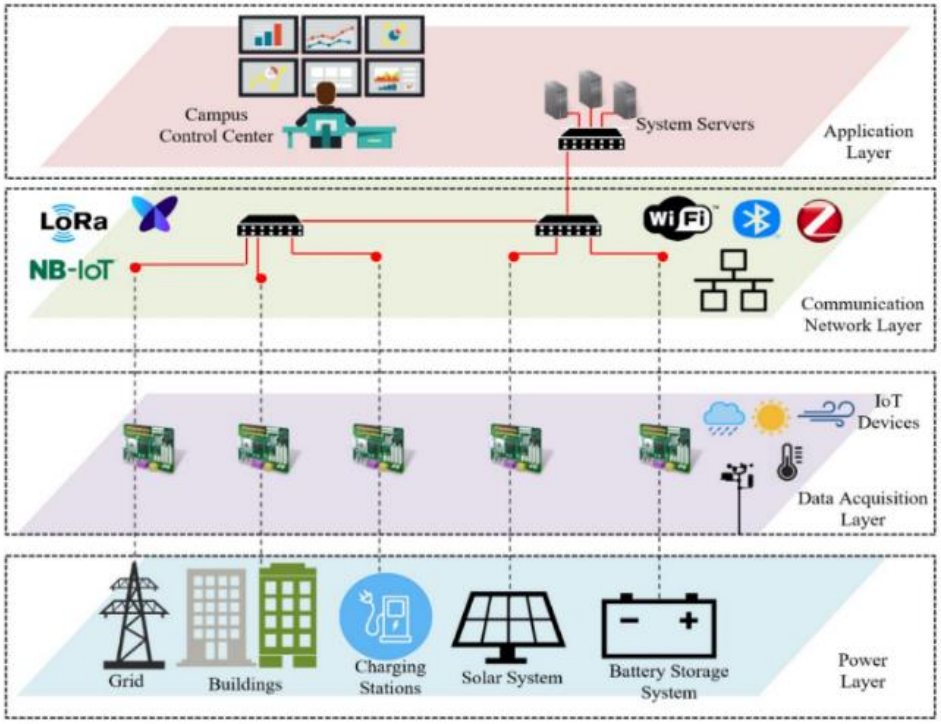

Fig. 5. Layered architecture of the proposed IoT-based environmental monitoring system

The cloud platform represents the final layer of the proposed IoT monitoring system and enables data storage, real-time visualization, and analysis of the measured environmental parameters through Supabase and a Vercel-based web dashboard [5].

After the environmental parameters are measured by the sensors, the data are processed by the ESP32 microcontroller and transmitted through the LoRa gateway. The gateway forwards the received data to the cloud backend, where the measurements are stored in a Supabase database.

Each measurement record includes the sensor node information, timestamp, and measured values such as particulate matter concentration, temperature, pressure, and noise level. This enables both real time monitoring and historical data analysis. The stored data are then accessed by a web dashboard deployed on Vercel, where the values are presented through cards, tables, and graphical representations. The platform allows users to observe current environmental conditions, analyze trends over the last 24 hours, and review daily or monthly changes. In addition, the system is designed to support comparison between different sensor nodes, which makes it suitable for future expansion into a distributed monitoring network across the university campus.

The left part in Figure 6. shows the 24-hour trend visualization of the measured environmental parameters through the web dashboard. The displayed graphs include noise level, $PM_{2.5}$ and PM_{10} particle concentrations, and ambient temperature. This visualization enables real-time monitoring and easier analysis of changes in the measured values over time. While the figure on the right shows the real-time display of the measured environmental parameters for one of the sensor nodes.

This view enables quick monitoring of the current environmental conditions at the selected location.

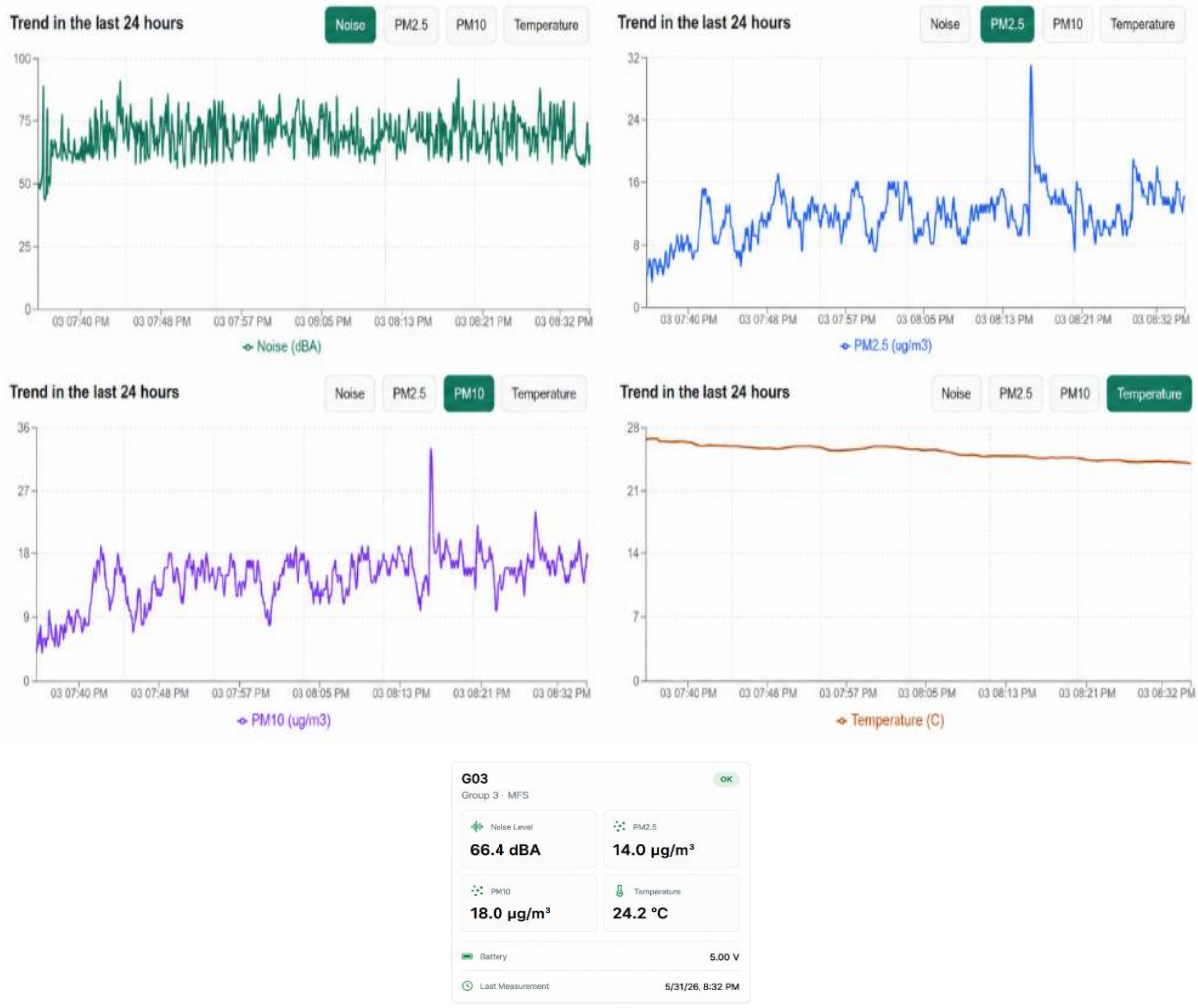

Fig. 6. Web dashboard trend visualization of measured environmental parameters

FRAMEWORK FOR A SINGLE SENSOR UNIT

Hardware architecture

The hardware architecture of the system is based on the integration of an ESP32 microcontroller with multiple environmental sensors. The components are interconnected through standard digital interfaces, enabling reliable data acquisition and communication. The selected hardware ensures a compact, low-cost, and scalable solution.

Table 1 below summarizes the technical specifications of the sensors used in the proposed system. The selected sensors provide reliable measurements of key environmental parameters, including particulate matter, temperature, pressure, and noise levels.

T a b l e 1

Technical specifications of the sensors used in the proposed system

Component	Parameter	Measurement method	Measuring range	Resolution/ Sensitivity	Accuracy	Interface	Supply voltage / power consumption
1. PMS5003	PM_1, $PM_{2.5}$, PM_{10}	Laser scattering principle	0 – 500 µg/m³	1 µg/m³	±10 µg/m³ or ±10%	UART	5 V / ~100 mA
2. BMP280	Temperature and pressure	MEMS – based sensing	−40 to +85°C; 300–1100 hPa	0.01°C; 0.18 Pa	±1 °C; ±1 hPa	I2C	5 V / ~100 mA
3. INMP441	Sound level	MEMS digital	~30 – 120 dB (estimated)	24-bit digital output	±1 dB (typical)	I2S	3.3 V / ~0.6 mA

The PMS5003 sensor is based on a laser scattering principle and can be used for low-cost particulate matter monitoring, although its performance should be evaluated against reference instruments for reliable environmental applications [6]. The BMP280 sensor integrates temperature, and pressure measurements in a compact MEMS-based design. While the INMP441 digital microphone enables accurate acquisition of environmental noise levels.

The ESP32 LoRa module serves as the central processing and communication unit, coordinating sensor operation, managing data acquisition, and transmitting the collected data to the network gateway.

Mechanical design of the sensor unit enclosure

The mechanical design of the sensor unit enclosure was developed to provide a compact and protective housing for the electronic components and sensors (Figure 7). The enclosure is intended to be manufactured using 3D printing technology.

Fig. 7. Mechanical design of the 3D-printed sensor unit enclosure

The enclosure includes dedicated openings and internal compartments for proper sensor placement, following the design principle that particulate matter sensors require unobstructed airflow through the enclosure for reliable measurements [7]. The particulate matter sensor requires direct airflow, while the noise sensor is positioned close to an external opening in order to detect ambient sound levels more accurately. The remaining electronic components, including the ESP32 LoRa module, power management modules, and battery, are placed inside the enclosure to protect them from external influences.

The proposed enclosure design supports easy installation on existing campus infrastructure, such as lighting poles, and contributes to the portability and scalability of the monitoring system.

SOFTWARE ARCHITECTURE

Power supply concept

The proposed sensor unit is designed to operate as a portable device, suitable for outdoor placement across the faculty campus. For this reason, the power supply concept (Figure 8) is based on three possible power sources: USB power during development and testing, a rechargeable lithium battery for autonomous operation, and a solar panel for extending the operating time of the system.

Fig. 8. Power supply concept of the proposed IoT sensor unit

The selected battery is a 26650 lithium-ion cell with a nominal voltage of 3.7 V and a capacity of 5000 mAh. The battery capacity was selected based on the estimated current consumption of the main components.

The ESP32 with LoRa communication, together with the PMS5003, BMP280, and INMP441 sensors, requires a current in the range of approximately 180–250 mA during active operation. For a 5000 mAh battery, the approximate operating time can be estimated as:

$$Operating\ time \approx \frac{Battery\ capacity}{Average\ current\ consumption}$$

because the battery voltage is lower than the voltage required by some components, a power management subsystem is included. The TP4056 module is used for safe charging of the lithium battery, while the MT3608 DC-DC step-up converter is used to increase the battery voltage and provide a stable 5V supply where needed. This is especially important for components such as the PMS5003 sensor, which operates at 5V.

A 5V, 3W solar panel is included as an additional charging source to support autonomous outdoor operation, following the concept of self-sustaining LoRaWAN-based air quality monitoring prototypes [8]. The solar panel is used to support the battery charging process and extend the operating time of the sensor unit when it is placed outdoors. This makes the system more suitable for long-term environmental monitoring, since it reduces the need for frequent manual charging.

SYSTEM EVALUATION AND VALIDATION APPROACH

Noise sensor calibration and validation

The calibration and validation of the INMP441 noise sensor were performed in the mechatronics laboratory by comparing its measurements with a reference sound level meter. During the experiment, sound signals with different frequencies were generated, while the values from both the INMP441 sensor and the reference instrument were recorded simultaneously. For each frequency, three measurements were taken with the proposed sensor and three measurements with the reference instrument. The average value was then calculated in order to reduce the influence of random variations and provide a more reliable comparison between the two devices.

From the obtained graph in Figure 9, it can be observed that the INMP441 sensor follows the same trend as the reference instrument. In the graph, *Series 1* represents the INMP441 sensor, while *Series 2* represents the reference sound level meter. The sensor shows stable behavior and can be used for monitoring changes in noise level.

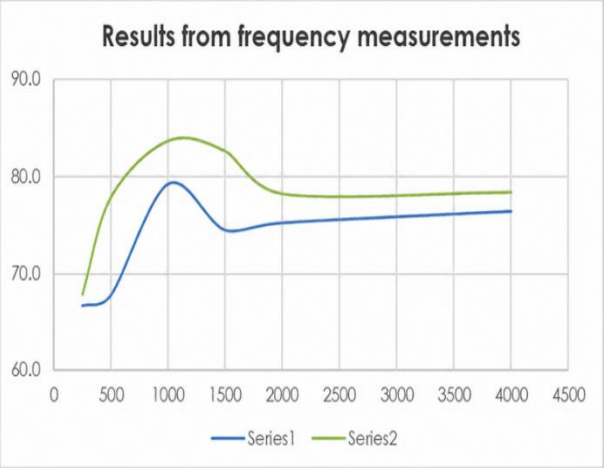

Fig. 9. Noise sensor validation at different sound frequencies

Noise sensor validation at different sound levels

Measurements were also performed at two different sound signal levels: low noise level and high noise level (Figure 10). For each level, three measurements were taken using the INMP441 sensor and three measurements using the reference sound level meter.

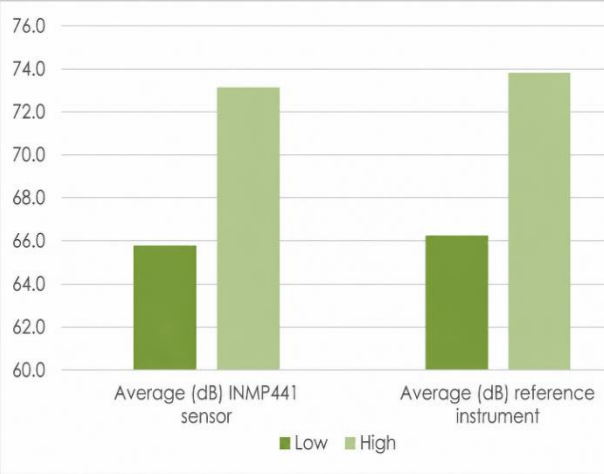

Fig. 10. Noise sensor validation at different sound levels

The average value was then calculated in order to obtain a more reliable comparison between the two devices.

Ambient noise level testing

The INMP441 sensor was also tested under ambient noise conditions in order to compare its measurements with the values obtained from the reference sound level meter.

The results showed in Figure 11 that the INMP441 sensor provides slightly lower values compared to the reference instrument. However, all measurements remain within a similar range. This indicates that the sensor can consistently detect ambient noise levels, although a certain deviation from the reference measurement is present. The observed difference may be caused by the microphone sensitivity, sensor positioning, and signal processing method.

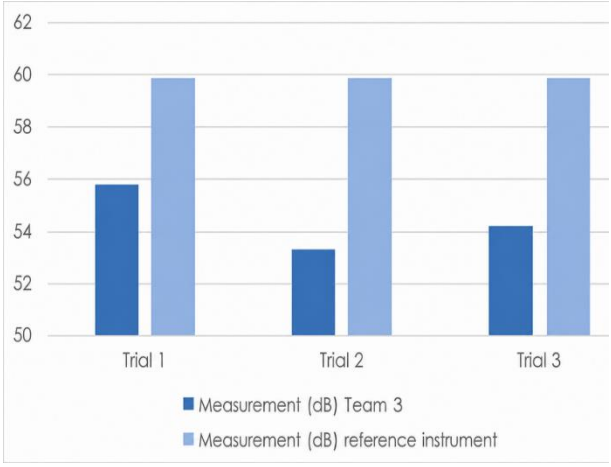

Fig. 11. Comparison of measured sound levels

The BMP280 temperature sensor would be evaluated by comparing its measurements with reference weather data or with a calibrated temperature sensor placed at the same location, following common validation approaches in which low-cost environmental sensors are assessed through simultaneous comparison with calibrated reference sensors [9]. The measurements will be performed over a defined time interval under real ambient conditions. The collected data would then be compared in order to determine whether the sensor follows the same temperature trend as the reference source. Possible deviations may occur due to local conditions such as sensor placement, airflow, shading, and the difference between point measurements and wider area weather data.

The PMS5003 sensor would be validated by comparing its $PM_{2.5}$ and PM_{10} measurements with official data from the State Automatic Ambient Air

Quality Monitoring System, operated by the Ministry of Environment and Physical Planning of the Republic of North Macedonia [10]. The sensor would be placed near an official reference monitoring station, where it would measure $PM_{2.5}$ and PM_{10} concentrations under the same ambient conditions as the reference station. The collected data would then be time aligned with the official measurements and compared in order to evaluate whether the proposed low-cost sensor follows the same trend as the reference system.

CONCLUSION

This work presented the design, development and preliminary validation of a low-cost IoT-based environmental monitoring system intended for smart campus applications. The integration of particulate matter, temperature, pressure, and noise sensors with an ESP32 LoRa module enabled real-time acquisition and wireless transmission of environmental data. The proposed cloud-based platform provided clear visualization of the measured parameters, allowing easier monitoring and analysis of environmental conditions overtime.

The developed sensor unit was designed as a modular and scalable solution, suitable for deployment at different locations across the faculty campus. The 3D-printed enclosure provided a compact housing for the electronic components while allowing proper exposure of the sensors to the surrounding environment. Testing of the noise sensor confirmed that the system follows the same general trend as the reference instrument, indicating its suitability for indicative monitoring and trend analysis.

Overall, the results highlight the effectiveness of combining low-cost sensors, wireless communication, cloud storage, and real-time visualization to create a practical environmental monitoring platform. For future work, we plan on focusing on long-term outdoor testing, further sensor calibration, power optimization, and deployment of multiple sensor nodes across the campus.

REFERENCES

[1] N.N.: *Air pollution*, World Health Organization, Available: https://www.who.int/health-topics/air-pollution

[2] Alam, M., Islam, M. M., Nayan, N. M., Uddin, J. (2024): An IoT based real-time environmental monitoring system for developing areas, *Journal of Advanced Research in Applied Sciences and Engineering Technology*, vol. **52**, No. 1, pp. 106–121. DOI: 10.37934/araset.52.1.106121

[3] Ramesh, P., Vidhya, N., Bhuvaneswari, P. T. V., Parveen, S. (2023): I-SOEWM: IoT based solar energized weather monitoring system, *Indian Journal of Science and Technology*, vol. **16**, No. 20, pp. 1505–1515. https://doi.org/10.17485/IJST/v16i20.287

[4] Uddin, M. S., Praharaj, M. K. (2025): IoT based weather monitoring system using ESP32 microcontroller, *International Journal of Advanced Research in Science Communication and Technology*. DOI: 10.48175/IJARSCT-29283 (2025).

[5] Petrică, S.-M., Făgărășan, I., Arghira, N., Munteanu, I. (2026): Real time IoT low-cost air quality monitoring system, *Sustainability*, vol. **18**, No. 2, 1074. DOI: 10.3390/su18021074

[6] Bulot, F. M. J., Russell, H. S., Rezaei, M., Johnson, M. S., Ossont, S. J. J., Morris, A. K. R., Basford, P. J., Easton, N. H. C., Foster, G. L., Loxham, M., Cox, S. J. (2020): Laboratory comparison of low-cost particulate matter sensors to measure transient events of pollution, *Sensors*, vol. **20**, No. 8, 2219. https://doi.org/10.3390/s20082219

[7] Mahajan, S., Gabrys, J., Armitage, J. (2021): AirKit: A citizen-sensing toolkit for monitoring air quality, *Sensors*, vol. **21**, No. 12, 4044. https://doi.org/10.3390/s21124044

[8] Balagopal, G., Wijeratne, L., Waczak, J., Lary, D. J. (2025): Calibration of low-cost LoRaWAN-based IoT air quality monitoring prototype, *Sensors*, vol. **25**, No. 5, 1614. https://doi.org/10.3390/s25051614

[9] Budiawan, I., Ananda, N., Wicaksana, H. S., Burohman, A. M., Mukhlish, F., Ekawati, E., Kurniadi, D. (2026): A study on environmental sensors for low-cost weather stations, *Engineering Innovations*, vol. **17**, pp. 57–74. DOI:10.4028/p-X0oD4Y

[10] Ministry of Environment and Physical Planning of the Republic of North Macedonia: Official website. Available: https://www.moepp.gov.mk/

Mechanical Engineering – Scientific Journal, Vol. **44,** No. 1, pp. 47–53 (2026)
Number of article: 704 ISSN 1857–5293
Received: May 12, 2026 e-ISSN 1857–9191
Accepted: June 10, 2026 UDC: 004.312.466:681.782.42
https://doi.org/10.55302/MESJ2644147a

Original scientific paper

DESIGN AND EXPERIMENTAL ANALYSIS OF LOW-COST AUTOMATED SOLAR TRACKING SYSTEM

Maja Anačkova, Mario Angjelkovski, Evgenija Jovanovska, David Pejovski, Filip Rajčevski

Faculty of Mechanical Engineering, "Ss. Cyril and Methodius" University in Skopje,
P.O. Box 464, MK-1001 Skopje, Republic of North Macedonia
maja.anachkova@mf.edu.mk

A b s t r a c t: This paper presents a low cost dual-axis light tracking prototype developed as a basis for future photovoltaic (PV) solar tracker systems. The device uses an Arduino microcontroller and four light resistors (LDRs) arranged in four sensing quadrants. The controller continuously samples and compares the quadrant signals to estimate the light direction and drives two SG90 servo motors to position the platform in azimuth and elevation. To improve stability and reduce unnecessary actuation, the control strategy applies averaged sensor sampling, differential error evaluation, and a tunable tolerance band (dead zone) that suppresses micro-adjustments under small intensity variations. This prototype is more energy efficient and simple to implement, making it suitable for educational demonstrations and preliminary research. Future work will integrate a photovoltaic module (solar panel) and external electrical measurements to quantify the improvements in energy yield over fixed – tilt configurations.

Key words: dual-axis tracker; Arduino; LDR sensors; closed-loop control; tolerance band

ДИЗАЈН И ЕКСПЕРИМЕНТАЛНА АНАЛИЗА НА НИСКОБУЏЕТЕН АВТОМАТИЗИРАН СИСТЕМ ЗА СЛЕДЕЊЕ НА СОНЦЕТО

А п с т р а к т: Во овој труд е претставен нискобуџетен прототип за двоосно следење на светлина, развиен како основа за идни фотоволтаични (PV) системи за следење на Сонцето. Уредот користи Arduino-микроконтролер и четири фотоотпорници (LDR), поставени во четири сензорски квадранти. Контролерот континуирано ги мери и споредува сигналите од квадрантите за да ја процени насоката на светлината и управува со два сервомотора SG90 за позиционирање на платформата по азимут и елевација. За подобрување на стабилноста и намалување на непотребното активирање, контролната стратегија применува просечно земање примероци од сензорите, процена на диференцијалната грешка и приспособување на опсегот на толеранција (мртва зона), со кој се потиснуваат микро-поместувањата при мали промени во интензитетот на светлината. Овој прототип е енергетски поефикасен и едноставен за имплементација, што го прави погоден за едукативни демонстрации и прелиминарни истражувања. Идната работа ќе вклучи интеграција на фотоволтаичен модул (соларен панел) и надворешни електрични мерења, со цел да се квантифицира подобрувањето на добиената енергија во споредба со конфигурации со фиксен агол на поставување.

Клучни зборови: двоосен следач; Arduino; LDR сензори; управување во затворена јамка; опсег на толеранција

INTRODUCTION

The increasing demand for electricity and the need to reduce the environmental impact of energy production have intensified interest in photovoltaic (PV) systems for residential and small scale applications. However, many PV installations are fixed (e.g., roof-mounted arrays), which leads to significant daily output variation due to the continuous change in the Sun's apparent position, panels

mounted on opposite roof sides may perform better at different times of the day, highlighting the limitations of static mounting [1].

Solar tracking systems reduce these losses by reorienting the PV surface toward the largest light source. Prior work ranges from simplified single-axis mechanisms to dual-axis closed-loop solutions. A dual-axis Arduino-based tracker using photodiodes with stepper and linear actuation reported approximately 18% higher energy yield compared to a static panel [2], while a low-cost dual – axis design based on LDR sensing and two servo motors achieved a reported 13.44% improvement over an immobile PV system. Despite these benefits, low – cost sensor driven trackers may exhibit oscillations and unnecessary micro movements under sensor noise and rapid illumination changes, which can reduce mechanical stability and increase wear [3].

In this paper, a low cost dual-axis light tracking prototype is developed as a foundation for future PV tracker integration. The system uses an Arduino microcontroller, four quadrant arranged LDR sensors, and two servo motors for azimuth and elevation control. Averaged sampling, differential error evaluation, and a tunable tolerance band are implemented to suppress unnecessary movements and improve stability, providing a modular platform for educational use and future outdoor PV performance measurements.

EXPERIMENTAL

System overview and hardware components

The proposed dual-axis light tracking prototype comprises a miniature solar panel, two SG90 servo motors, four light-dependent resistors (LDRs), an Arduino Uno microcontroller, an LCD display, and a 3D-printed mechanical structure as shown in Figure 1.

The mechanical assembly provides two orthogonal degrees of freedom (horizontal/azimuth and vertical/elevation), enabling the panel to be oriented toward the dominant light direction. The device is powered from a 5V supply.

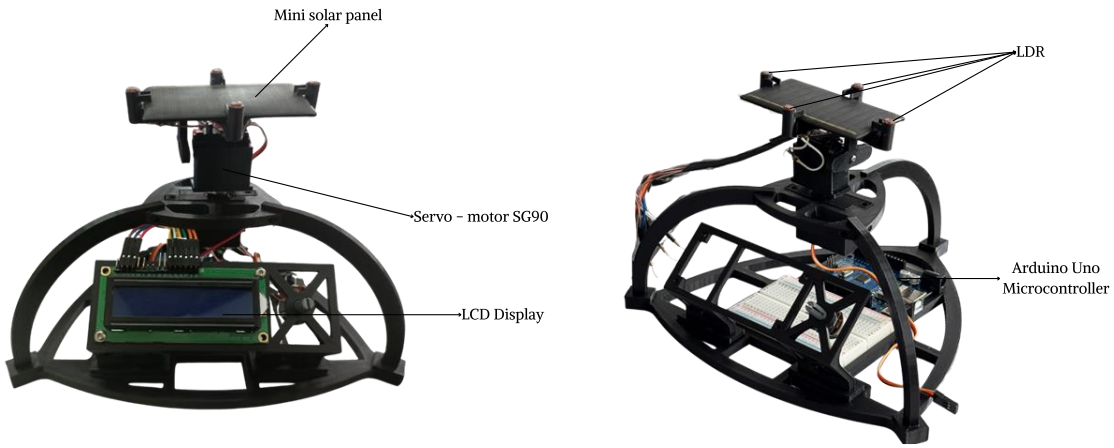

Fig. 1. Developed dual-axis solar tracking prototype with main components

Mechanical construction and fabrication

The supporting frame was 3D printed, using PLA for the main structure and PETG for the moving parts to improve wear resistance. A CAD model defined the precise assembly interfaces between the servos and the panel mount (Figure 2).

Four vertical walls separate the LDR sensors on the top mount, forming what are referred to as quadrant shadow casters. When the light source is off-axis, these walls cast a shadow over the sensors facing away from it, while the sensors facing toward it remain fully exposed. The resulting intensity difference between opposing sensors produces the differential signal used to drive the servo motors [4].

Due to the tracker's compact geometry, the design lacks physical end-stops, risking mechanical collision at extreme elevation angles. To prevent structural damage and actuator stalling, all rotational constraints are strictly enforced through the microcontroller's software logic.

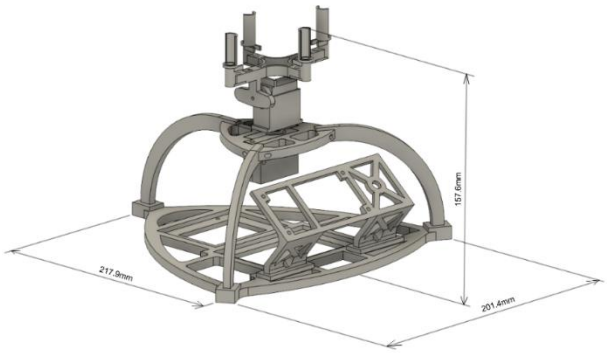

Fig. 2. CAD model of the 3D-printed mechanical structure of the dual-axis solar tracker with overall dimensions (mm)

Sensor configuration and signal acquisition

Light sensing is implemented using four LDR5 photoresistors arranged in a cross configuration (top, bottom, left, right). Each LDR forms a voltage divider with a fixed 10 kΩ resistor, producing an analog voltage proportional to incident light intensity (Figure 3).

The four divider outputs are connected to the Arduino Uno analog inputs A0 – A3. The built-in 10-bit analog-to-digital converter (ADC) converts these voltages into digital values in the range 0 – 1023. The selected LDR characteristics are suitable for dynamic tracking applications, with peak spectral sensitivity around 540 nm and response times of approximately 20 ms (rise) and 30 ms (fall). The typical resistance transitions from a high dark resistance (≤ 500 kΩ) to a lower illuminated resistance (approximately 5 – 10 kΩ), enabling reliable discrimination of light differences between quadrants within the operating temperature range of −30 °C to +70 °C.

To reduce the influence of sensor tolerances and shorts term fluctuations, the sampled readings are processed in software using averaging and calibration steps before being used by the control logic. The processed sensor values represent the relative illumination in each quadrant and serve as the system's input for determining the required orientation corrections.

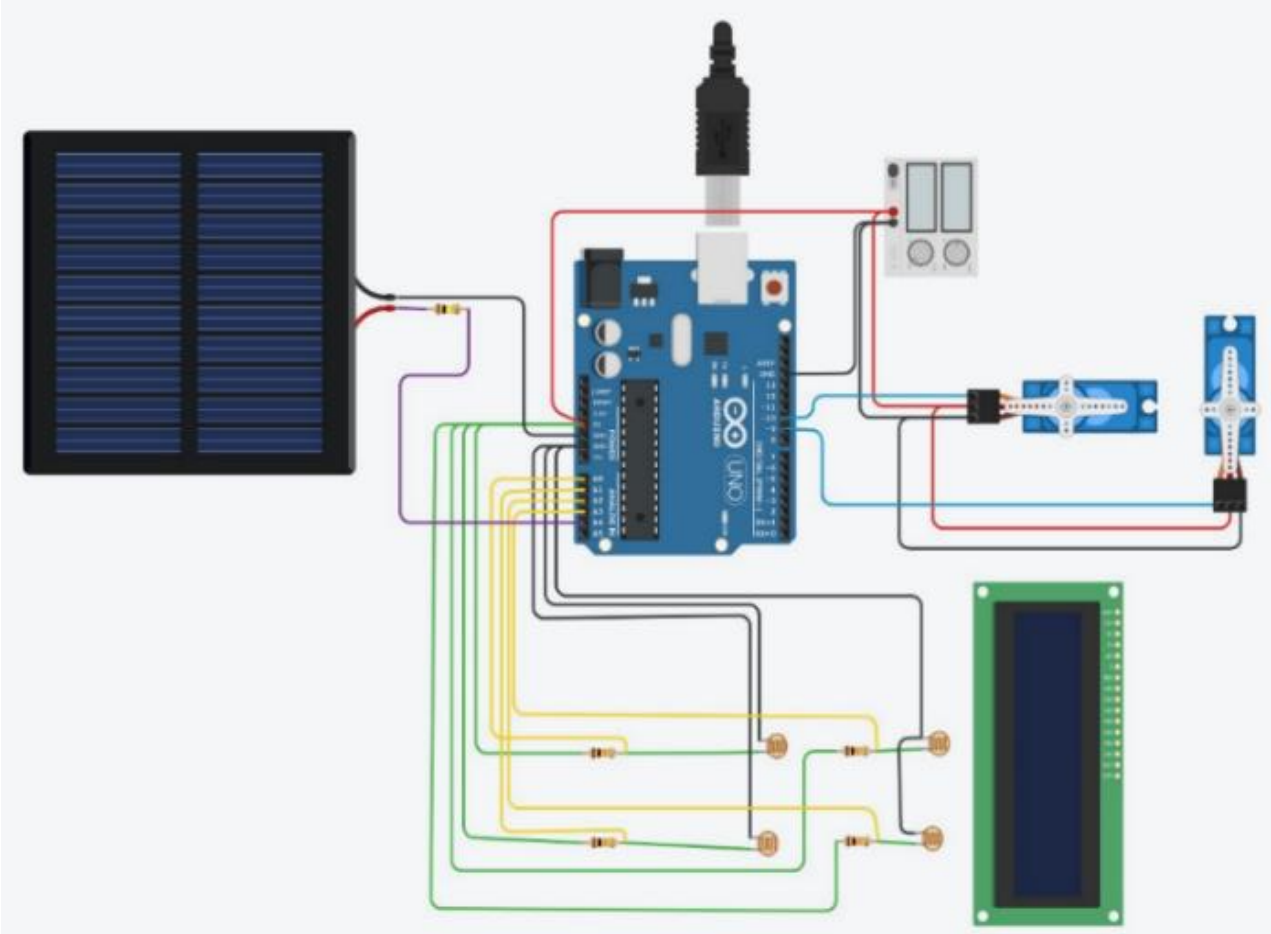

Fig. 3. Electrical wiring diagram of the dual-axis solar tracking system implemented in TinkerCad

Control algorithm

The control strategy (Figure 4) is based on pairwise comparison of quadrant sensors. Horizontal correction is determined from the difference between the left and right LDR readings, while vertical correction is determined from the difference between the top and bottom readings.

If the absolute difference between a sensor pair exceeds a predefined dead-zone (tolerance threshold), the controller commands a small angular step toward the brighter side. If the difference remains within the dead-zone, no motion is executed, which suppresses unnecessary micro-adjustments and improves stability.

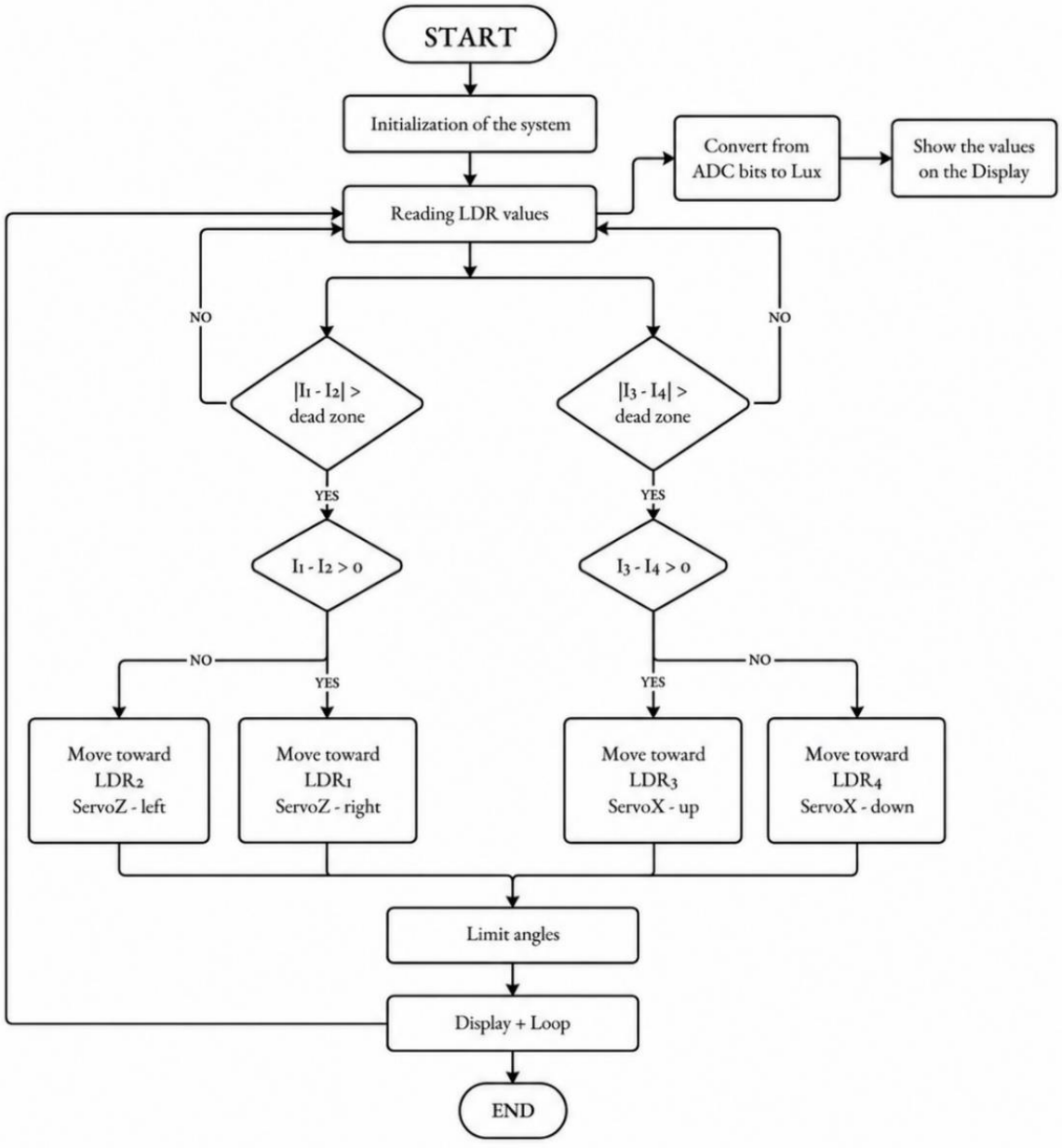

Fig. 4. Flowchart of the dual-axis solar tracking control algorithm

Safety limits are applied to constrain the minimum and maximum servo angles especially for the vertical axis to prevent mechanical interference and damage. In addition, protective transition logic is implemented when moving between extreme positions to avoid rapid back-and-forth behavior and oscillations. This ensures stable operation under varying illumination conditions and avoids continuous actuator activity caused by small sensor noise.

Actuation and motion strategy

The actuation is done by two servo motors controlled by an Arduino Uno microcontroller (Figure 5). ServoX controls the elevation using the difference between the top and bottom LDRs. While ServoZ controls the azimuth using the difference between the left and right LDRs. In case the ServoZ motor exceeds its mechanical limits, a so-called flip maneuver is activated. Where 180° is subtracted from the values of both motors.

When the flip maneuver is performed, there is a small angular limitation so that it does not return back, in order to avoid oscillation of the flip maneuver.

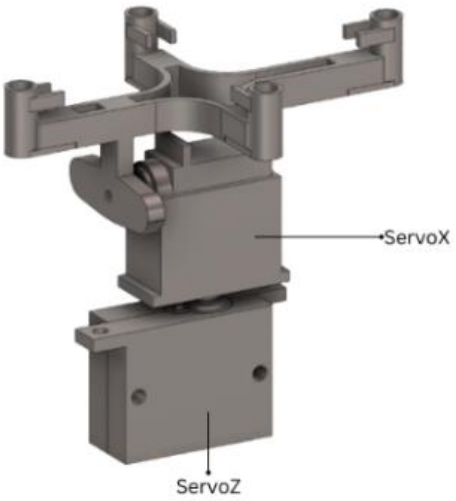

Fig. 5. Actuation mechanism of the proposed solar tracking prototype

RESULTS

Light intensity measurements

To determine the relative sensitivity of the photoresistors used in the system, a controlled experimental measurement was performed. An electric lamp of known characteristics was used as a light source and positioned so that the light beam fell directly and approximately perpendicularly on the surface of the photoresistors, thus minimizing the influence of the angle of illumination.

The experiment was carried out by gradually changing the distance between the light source and the LDRs. We first measured the distance from the light source, and then the distance from it to see if hysteresis would occur. The measurements were carried out at the following distances: 15, 30, 45, 60, 75, 90, 105, 120, 135, 150, 165, 180, 195, 210, 225, 240 cm. To improve accuracy and reduce random deviations, measurements were repeated three times under the same conditions. The results are presented in Figure 6.

The result from the graph shows that the increasing and decreasing measurements show no measurable hysteresis and follows an exponential curve.

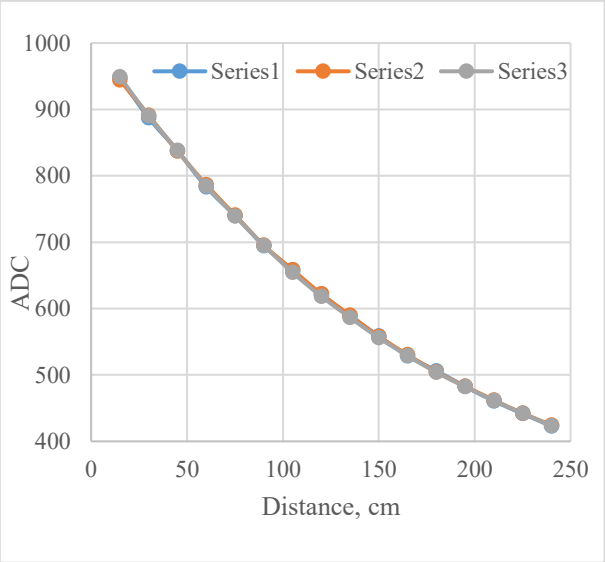

Fig. 6. LDR response during increasing and decreasing distance measurements

The second graph, Figure 7 (from the second experiment) shows a full-day outdoor test of the solar tracking system. The test was conducted to evaluate the real-time performance, stability, and reliability of the system under actual outdoor operating conditions.

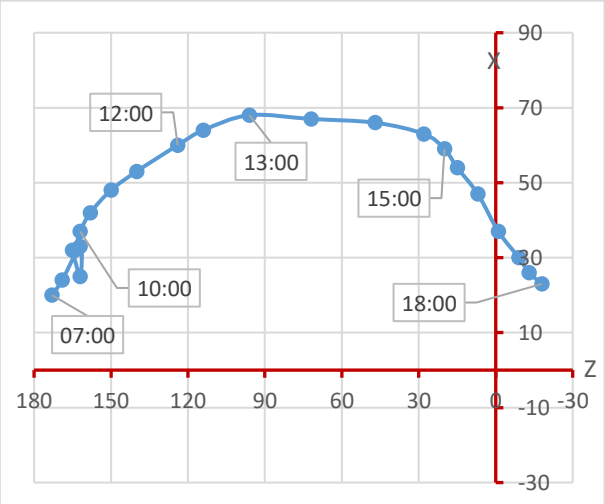

Fig. 7. Measured angular trajectory of the dual-axis solar tracking system during outdoor testing

From the graph, it can be observed that the tracker accurately followed the Sun's trajectory across the sky from 07:00 to 18:00. The gradual change of the tracking angle during the day confirms that the system continuously adjusted its position according to the movement of the Sun.

Finally, the third graph, Figure 8 demonstrates the advantage of such a system, showing how solar tracking can improve the overall efficiency of the panel compared to a fixed-position setup. The experiment was performed using two methods: a stationary setup and an active solar tracking setup.

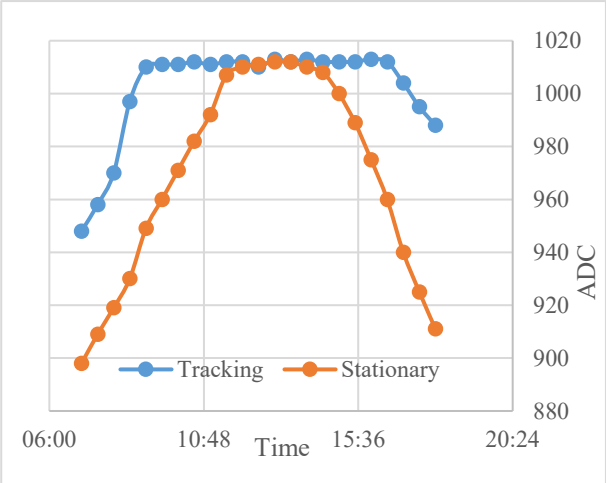

Fig. 8. Comparison of light intensity between tracking and stationary setup during the day

The measured light-intensity profile shows better performance when the device actively tracked the Sun compared to the stationary control setup. The readings are presented as ADC values, which represent the sensor output voltage.

Measurement of speed and response time

To determine the response speed, an experiment was conducted in which an angular displacement of 90 degrees resulted in an average response time of approximately 1 second, corresponding to about 11 ms per degree. Since the measurements were performed manually, involving two operators, the experiment was repeated five times in order to account for possible human error. The most repeatable measurement was selected as the representative value, as it was closest to the value defined in the program.

Overshoot

Figure 9 shows the occurrence of overshoot during a sudden change in illumination, where the signal exceeds the set dead zone (from –16 to 16ADC bits).

The overshoot is short-lived and the system quickly stabilizes, indicating a stable but fast response of the control system.

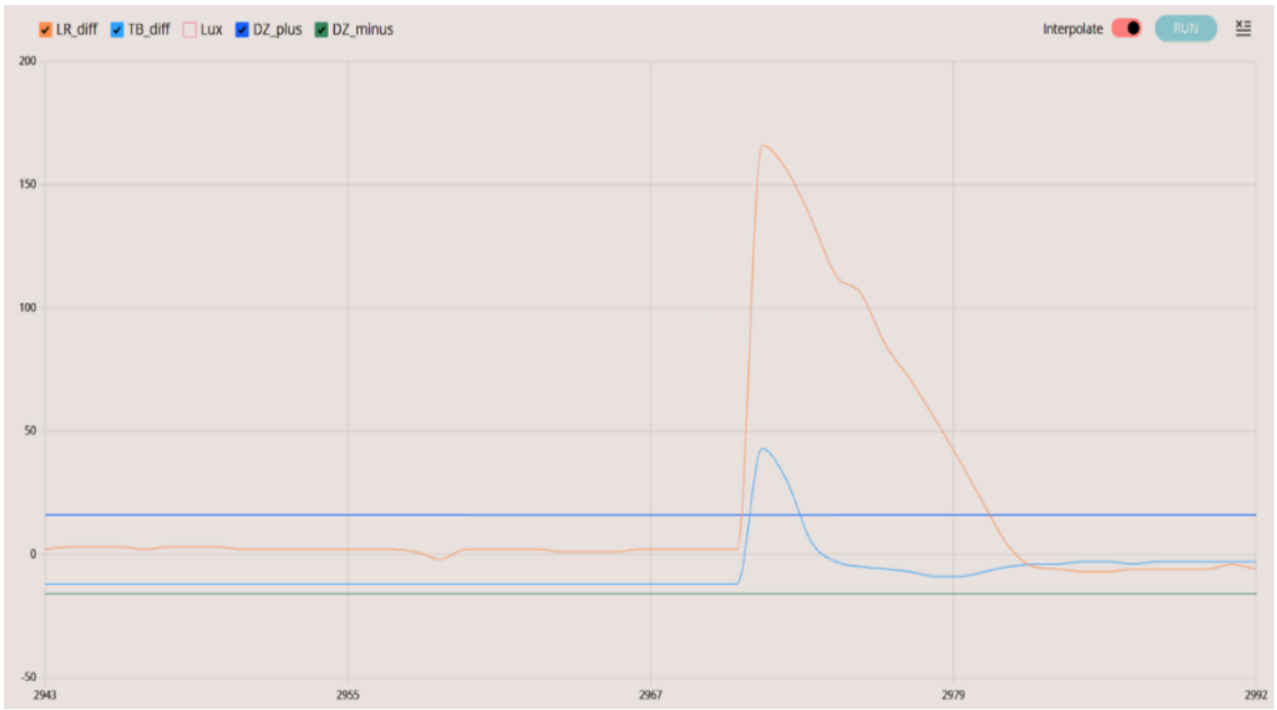

Fig. 9. Overshoot in differential control signal during rapid light variation

Display latency

In this system, latency does not refer to the control algorithm or the servo motor response, but to the update rate of the values shown on the LCD. Due to LCD module limitations and the requirement for the information to remain readable to the user, the displayed values are not updated continuously; instead, they are refreshed periodically, approximately every 480 ms.

This interval was selected as a compromise between update speed and human visual perception, since excessively fast updates make changes difficult to observe on the screen.

CONCLUSION

Within this project, a dual-axis automatic light -tracking system was designed and implemented using photoresistors and an Arduino microcontroller platform. The system processes sensor signals and controls servo motors to continuously adjust the panel orientation according to the light source.

Experimental measurements confirmed the functionality and sensitivity of the sensors, as well as the expected relationship between light intensity and distance from the source. The results indicate stable system response to illumination changes and successful position correction.

Although the system requires additional mechanical optimization and maintenance, it represents a practical solution for small-scale and educational applications. Future work will focus on improving the voltage divider design, upgrading the controller platform, enabling wireless monitoring, and comparing the real energy yield of the tracking system with a fixed reference setup.

Acknowledgement. The authors would like to thank the Faculty of Mechanical Engineering in Skopje, as well as the mentors and colleagues who provided support, guidance, and technical assistance during the development and testing of this prototype.

REFERENCES

[1] Alijanov, D. D., Topvoldiyev, N. A. (2021): Solar tracker system using Arduino, *ISJ Theoretical & Applied Science*, Vol **101** (9), pp. 249–253, DOI: 10.15863/TAS.2021.09.101.18

[2] Morón, C., Ferrández, D., Saiz, P., Vega, G., Díaz, J. P. (2017): New prototype of photovoltaic solar tracker based on Arduino, *Energies*, vol. **10**, No. 9, 1298. DOI: https://doi.org/10.3390/en10091298

[3] Kaur, T., Mahajan, S., Verma, S., Gambhir, J. (2016): Arduino based low cost active dual axis solar tracker, *Proceedings of the 2016 IEEE 1st International Conference on Power Electronics, Intelligent Control and Energy Systems (ICPEICES)*, pp. 1–5.

[4] Wang, J. M., Lu, C. L. (2013): Design and implementation of a sun tracker with a dual-axis single motor for an optical sensor-based photovoltaic system, *Sensors*, Vol. **13**, No. 3, pp. 3157–3168. https://doi.org/10.3390/s130303157

Mechanical Engineering – Scientific Journal, Vol. **44,** No. 1, pp. 55–58 (2026)
CODEN: MINSC5
In print: ISSN 1857–5293
On line: ISSN 1857–9191

INSTRUCTIONS FOR AUTHORS

The *Mechanical Engineering – Scientific Journal* is published twice yearly. The journal publishes **original scientific papers, short communications, reviews** and **professional papers** from all fields of mechanical engineering.

The journal also publishes (continuously or occasionally) the bibliographies of the members of the Faculty, book reviews, reports on meetings, informations of future meetings, important events and data, and various rubrics which contribute to the development of the corresponding scientific field.

Original scientific papers should contain hitherto unpublished results of completed original scientific research. The number of pages (including tables and figures) should not exceed 15 (28 000 characters).

Short communications should also contain completed but briefly presented results of original scientific research. The number of pages should not exceed 5 (10 000 characters) including tables and figures.

Reviews are submitted at the invitation of the Editorial Board. They should be surveys of the investigations and knowledge of several authors in a given research area. The competency of the authors should be assured by their own published results.

Professional papers report on useful practical results that are not original but help the results of the original scientific research to be adopted into scientific and production use. The number of pages (including tables and figures) should not exceed 10 (18 000 characters).

Acceptance for publication in the Journal obliges the authors not to publish the same results elsewhere.

SUBMISSION

The article and annexes should be written on A4 paper with margins of 2.5 cm on each side with a standard font Times New Roman 11 points and should be named with the surname of the first author and then if more and numbered. It is strongly recommended that on MS Word 2003 or MS Word 2007 and on PDF files of the manuscript be sent by e-mail:

mesj@mf.edu.mk.

A letter must accompany all submissions, clearly indicating the following: title, author(s), corresponding author's name, addres and e-mail addres(es), suggested category of the manuscript and a suggestion of five referees (their names, e-mail and affiliation).

Articles received by the Editorial Board are sent to two referees (one in the case of professional papers). The suggestions of the referees and Editorial Board are sent to the author(s) for further action. The corrected text should be returned to the Editorial Board as soon as possible but in not more than 30 days.

PREPARATION OF MANUSCRIPT

The papers should be written in the shortest possible way and without unnecessary repetition.

The original scientific papers, short communications and reviews should be written in English, while the professional papers may also be submitted in Macedonian.

Only SI (Système Internationale d'Unites) quantities and units are to be used.

Double subscripts and superscripts should be avoided whenever possible. Thus it is better to write $\nu_3(PO_4)$ than $\nu_{3_{PO_4}}$ or exp(–E/RT) than $e^{-E/RT}$. Strokes (/) should not be used instead of parentheses.

When a large number of compounds have been analyzed, the results should be given in tabular form.

Manuscript should containt: title, author(s) full-name(s), surname(s), address(es) and e-mail of the corresponding author, short abstract, key words, introduction, experimental or theoretical background, results and discussion, acknowledgment (if desired) and references.

The **title** should correspond to the contents of the manuscript. It should be brief and informative and include the majority of the key words.

Each paper should contain an **abstract** that should not exceed 150 words, and **3–5 key words**. The abstract should include the purpose of the research, the most important results and conclusions.

The **title**, **abstract** and **key words** should be translated in Macedonian language. The ones written by foreign authors will be translated by the Editorial Board.

In the **introduction** only the most important previous results related to the problem in hand should be briefly reviewed and the aim and importance of the research should be stated.

The **experimental** section should be written as a separate section and should contain a description of the **materials used and methods** employed – in form which makes the results reproducible, but without detailed description of already known methods.

Manuscripts that are related to **theoretical studies**, instead of experimental material, should contain a sub-heading and the **theoretical background** where the necessary details for verifying the results obtained should be stated.

The **results and discussion** should be given in the same section. The discussion should contain an analysis of the results and the conclusions that can be drawn.

Figures (photographs, diagrams and sketches) and **mathematical formulae** should be inserted in the correct place in the manuscript, being horizontally reduced to 8 or 16 cm. The size of the symbols for the physical quantities and units as well as the size of the numbers and letters used in the reduced figures should be comparable with the size of the letters in the main text of the paper. Diagrams and structural formulae should be drawn in such a way (e.g. black Indian ink on white or tracing paper) as to permit high quality reproduction. The use of photographs should be avoided. The tables and the figures should be numbered in Arabic numerals (e.g., Table 1, Figure 1). Tables and figures should be self-contained, i.e. should have captions making them legible without resort to the main text. The presentation of the same results in the form of tables and figures (diagrams) is not permitted. The use of equation editor (MS Word, Microsoft Equation, Math Type 6.0 Equation) for typesetting the equations is recommended. Strokes (/) should not be used instead of parentheses.

Figures and tables must be centred in the column. Large figures and tables may span across both columns (Figure 1).

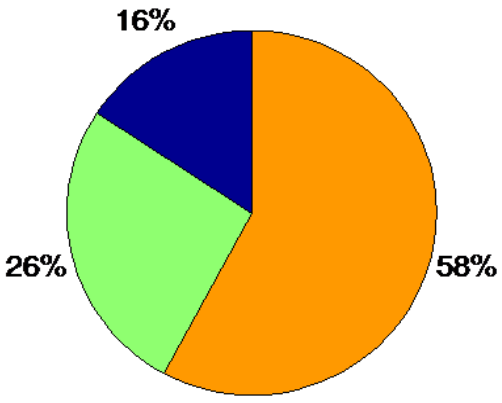

Fig. 1. Example of a graph and a single-line caption (colour)

Graphics may be full colour. Please use only colours which contrast well both on screen and on a black-and-white hardcopy because the Journal is published in black-and-white, as shown in Figure 2. The colour version is only for the electronic version of the Journal.

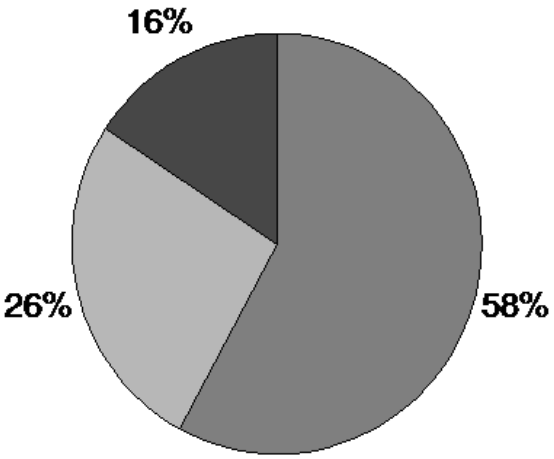

Fig. 2. Example of a graph and a single-line caption (bleck and white)

Please check all figures in your paper both on screen and on a black-and-white hardcopy. When you check your paper on a black-and-white hardcopy, please ensure that:

– the colours used in each figure contrast well (Figure 3),

– the image used in each figure is clear,

– all text labels in each figure are legible.

Please check all figures in your paper both on screen and on a black-and-white hardcopy. When you check your paper on a black-and-white hardcopy, please ensure that the image used in each figure is clear and all text labels in each figure are legible.

Fig. 3. Example of an image as it will appear at the electronic version of the Journal and a multi-line caption

Footnotes are also not permitted.

The **reference** should be given in a separate section in the order in which they appear in the text. The surname of one or two authors may be given in the text, whereas in the case of more than two authors they should be quoted as, for example:

Examples of reference items of different categories shown in the References section include:

- example of a book in [1]
- example of a book in a series in [2]
- example of a journal article in [3]
- example of a conference paper in [4]
- example of a patent in [5]
- example of a website in [6]
- example of a web page in [7]
- example of a databook as a manual in [8]
- example of a datasheet in [9]
- example of a master/Ph.D. thesis in [10]
- example of a technical report in [11]
- example of a standard in [12]

All reference items must be in 9 pt font. Please use Regular and Italic styles to distinguish different fields as shown in the References section. Number the reference items consecutively in square brackets (e.g. [1]).

When referring to a reference item, please simply use the reference number, as in [2]. Do not use "Ref. [3]" or "Reference [3]" except at the beginning of a sentence, e.g. "Reference [3] shows …". Multiple references are each numbered with separate brackets (e.g. [2], [3], [4–6]).

The **category** of the paper is proposed by the author(s), but the Editorial Board reserves for itself the right, on the basis of the referees' opinion, to make the final choice.

Proofs are sent to the author(s) to correct printers' errors. Except for this, alterations to the text are not permitted. The proofs should be returned to the Editorial Board in 2 days.

The author(s) will receive, free of charge, 1 reprints of every paper published in the Journal.

REFERENCES

[1] Surname, N(ame).; Surname, N(ame). (Year): *Name of the Book*, Publisher.

[2] Surname, N(ame).; Surname, N(ame). (Year): *Name of the Book*, Name of the Series. Publisher, **vol.** XXX.

[3] Surname, N(ame).; Surname N(ame). (Year): Title of the article, *Name of the Journal*, **vol. XX,** No. XX, pp. XXX–XXX.

[4] Surname, N(ame).; Surname N(ame). (Year): Title of the article, *Proceedings of the Name of the Conference,* vol. **XX,** pp. XXX–XXX.

[5] Surname, N(ame).; Surname, N(ame).: *Name of the Patent*, Institution that issued the patent and Number of the patent (Date dd. mm. yyyy).

[6] N.N. (Year): *The XXX web site*, web address.

[7] Surname, N. (Year): *XXX homepage on XXX*, web address.

[8] N.N. (Year): *Title of the Manual*, Name of the Organization.

[9] N.N.: *XXX data sheet*, Name of the Organization.

[10] Surname, N. (Year): *Title of the Thesis*, Master/Ph.D. thesis (in Language), Institution.

[11] Surname, N(ame).: Surname, N(ame). (Year): *Title of the Report*, Organization that issued the report, number of the report.

[12] Institution that issued the standard (Year): *Name of the Standard* & Number of the standard.